

# **MECH 498 - HONOURS THESIS**

## **OPTICAL PROPERTIES CHARACTERIZATION OF CZT SEMICONDUCTORS**



DEPARTMENT OF MECHANICAL ENGINEERING

Silvia Penkova  
V00733929

April 20, 2014

Supervisor: Dr. Thomas Tiedje  
Electrical and Computer Engineering

## Abstract

Cadmium Zinc Telluride ( $\text{Cd}_{1-x}\text{Zn}_x\text{Te}$ ) is a wide band gap semiconductor used for gamma and x-ray detection. CZT, a pseudo binary compound made up of CdTe and ZnTe, forms a face centered cubic zinc blend structure. A unique property of CZT is its tuneable lattice parameter. The lattice parameter depends on the zinc concentration. CZT crystals are grown by the travelling heater method in a  $\langle 111 \rangle$  orientation.

Samples with 4% and 10% zinc concentration were provided by UVIC Crystal Growth Group and Redlen Technologies, respectively. These were characterized using the methods of X-ray diffraction, photoluminescence, scanning electron microscopy and IR transmission. X-ray diffraction (XRD) allowed for a calculation of the lattice parameter and zinc concentration, as well as providing the offset from the  $\langle 111 \rangle$  growth direction. Photoluminescence (PL) enabled a direct measurement of the semiconductor band gap, which can be also used as a method for confirming the zinc concentration. In addition, the observed PL intensity is an indicator of the irregularities in the crystal lattice. Scanning electron microscopy and IR transmission allowed for imaging of the surface and internal structure of the samples which supported the performance results observed with XRD and PL.

The findings of the thesis are that 2% Bromine Methanol etch had an improvement on the PL intensity and reduced the XRD line width. This resulted because the polishing and etching smoothed out the surface from defects (XRD improvement) and removed oxidization (PL improvement). In addition, it was confirmed that the better performance of Detector 6, compared to Detector 8, was a result of the smoother surface (SEM images) and less irregularities in the crystal lattice (IR Transmission results).

## Table of Contents

1	Introduction .....	6
2	Cadmium Zinc Telluride .....	6
2.1	Structure.....	6
2.2	Growth Methods .....	7
2.3	Uses.....	7
2.4	Etching Process.....	7
3	High Resolution X-Ray Diffraction .....	8
3.1	Theory.....	8
3.1.1	X-ray Diffraction and the Bragg Condition .....	8
3.1.2	HRXRD Experiment Setup .....	9
3.1.3	Determination of Zinc Concentration .....	10
3.2	XRD Measurements – 10% Redlen Material .....	11
3.2.1	Data from Redlen Technologies.....	11
3.2.2	Non-Etched Samples Analysis .....	11
3.2.3	Etched Samples Analysis .....	12
3.3	XRD Measurements – 4% UVIC Crystal Growth Material .....	13
3.3.1	Effect on XRD Line Width With Etching.....	13
3.3.2	XRD FWHM Values With $2\theta$ - $\omega$ and $\omega$ - $2\theta$ Scans .....	14
4	Photoluminescence .....	15
4.1	Theory.....	15
4.2	Photoluminescence Experimental Setup.....	16
4.2.1	Optical Setup .....	17
4.3	Photoluminescence Measurements .....	19
4.3.1	Non-Etched Samples Analysis .....	19
4.3.2	Etched Sample Analysis.....	21
4.4	Zinc Concentration .....	24
5	Scanning Electron Microscopy.....	25
5.1	Theory.....	25
5.1.1	Scanning Electron Microscope Setup .....	25
5.1.2	Scanning Electron Microscope Imaging and Composition analysis .....	26
5.2	SEM Measurements .....	26
5.2.1	Chemical Composition.....	27
5.2.2	Surface Pictures .....	28
6	IR Transmission .....	29
6.1	Theory.....	29
6.1.1	Imaging with IR Transmission.....	29

6.1.2	IR Transmission Setup .....	30
6.2	IR Transmission Measurements.....	31
7	Discussion .....	33
7.1	Etched vs. Non Etched Results.....	33
7.1.1	X-ray Diffraction.....	33
7.1.2	Photoluminescence.....	34
7.2	Zinc Concentration Comparison.....	34
7.3	XRD Line Width and Surface/Internal Quality .....	35
7.3.1	Surface Quality.....	35
7.3.2	Internal Quality .....	35
7.4	Photoluminescence Intensity and Surface/Internal Quality.....	36
7.4.1	Surface Quality.....	36
7.4.2	Internal Quality .....	36
8	Conclusion.....	36
9	References .....	37
10	Appendix A – DCRC Measurement Technique [9] .....	39
11	Appendix B – HRXRD Data Non Etched .....	1
11.1	Detector 6 Non Etched XRD Data.....	1
11.2	Detector 8 Non Etched XRD Data.....	1
12	Appendix C – XRXRD Data Etched Samples .....	2
12.1	Detector 6 Etched XRD Data.....	2
12.2	Detector 8 Etched XRD Data.....	2
12.3	Samples 1218-3 Etched XRD Data .....	3
12.4	Sample 1527-9 Etched XRD Data.....	3
13	Appendix D – UVIC Crystal Growth Samples XRD Data .....	4
13.1	Crystal 3 – 5 min 2% Bromine Methanol Etch.....	4
13.2	Crystal 3 – 8 min 2% Bromine Methanol Etch.....	4

## Table of Figures

Figure 1:	CZT samples Detectors 6 and 8 used in characterization analysis.....	6
Figure 2:	Bragg's law definition [4] .....	8
Figure 3:	Bruker D8 Discover diffractometer system analyzing a CZT sample .....	9
Figure 4:	XRD beam optics set up showing analyzer crystal as part of the machine configuration [11] .....	10
Figure 5:	Double peak seen in XRD rocking curve scan of sample 1218-3.....	13

Figure 6: FWHM of 68.8692 arc seconds obtained with $2\theta-\omega$ scan.....	14
Figure 7: FWHM of 32.0213 arc seconds obtained with $\omega-2\theta$ scan.....	14
Figure 8: $\omega$ offset concept in reciprocal space [11] .....	15
Figure 9: Process flow diagram for exciting an electron in the conduction band and triggering a photon used to study the material in the electron/hole recombination process [12].....	16
Figure 10: Photoluminescence set up used for experiment.....	17
Figure 11: Range of acceptance angles in a fiber optic cable required to undergo internal reflection and transmit a signal .....	18
Figure 12: Typical monochromator set up showing how light it split into different wavelengths using a diffraction grating [14] .....	18
Figure 13: Intensity vs. Wavelength PL plot for a 10 second exposure time .....	20
Figure 14: Intensity vs. Energy plot for CZT samples at a 10 second exposure time ....	21
Figure 15: Etched samples PL data intensity vs. wavelength plot (1 second exposure). 22	
Figure 16: Etched samples PL intensity vs. wavelength plot (10 second exposure) .....	22
Figure 17: Etched samples Intensity vs. Energy plot (1 second exposure).....	23
Figure 18: Etched samples Intensity vs. Energy plot (10 second exposure).....	23
Figure 19: Scanning Electron Microscope internal diagram [16].....	25
Figure 20: Hitachi S-3500N Scanning Electron Microscope at UVIC .....	26
Figure 21: Location map of the spots used in SEM analysis of Detectors 6 and 8 .....	27
Figure 22: Qualitative spectral analysis results for Detector 6 .....	27
Figure 23: Qualitative spectral analysis results for Detector 8 .....	28
Figure 24: SEM images of Detector 6 at 100x magnification .....	28
Figure 25: SEM images of Detector 8 100x magnification .....	29
Figure 26: IR Transmission microscope at UVIC Crystal Growth Lab .....	30
Figure 27: Internal image of Detector 8 showing dislocations and Tellurium inclusions	31
Figure 28: Surface, middle and bottom IR transmission images of Detector 6 .....	32
Figure 29: Surface, middle and bottom IR transmission images of Detector 8 .....	32

## List of Tables

Table 1: Sample information from Redlen Technologies [19] .....	11
Table 2: Measured and calculated values for non-etched samples using data from XRD	12
Table 3: Measured and calculated values for etched samples using data from XRD.....	12
Table 4: Values of FWHM after different time intervals of etching .....	13
Table 5: Zinc concentration estimation from PL analysis .....	24
Table 6: Values comparing non-etch and etched FWHM results after 2 min 2% BrMeth etch.....	33
Table 7: Values comparing FWHM results after different times of 2% BrMeth etching	33
Table 8: Zinc concentration comparison between XRD and PL results .....	35

## 1 INTRODUCTION

The MECH 498 Honours Thesis focused on characterizing the optical properties of Cadmium Zinc Telluride semiconductors. Samples with 4% and 10% Zinc concentration were provided by UVIC Crystal Growth and Redlen Technologies, respectively. These were characterized using the methods of X-ray diffraction, photoluminescence, scanning electron microscopy and IR transmission. The samples were compared to each other for performance. This report serves to present the theory and discuss the findings of the thesis.

## 2 CADMIUM ZINC TELLURIDE

### 2.1 STRUCTURE

Cadmium Zinc Telluride ( $\text{Cd}_{1-x}\text{Zn}_x\text{Te}$ ) is a pseudo binary compound made up of CdTe and ZnTe which forms a face centered cubic (fcc) Zinc blend structure [1]. A unique property of CZT is its tuneable lattice parameter. The lattice parameter spacing is dependent on the Zinc concentration.

The level of Zinc concentration also has a direct effect on the band gap of the material. CZT has a wide band gap of 1.49 eV when compared with other semiconductors in the industry such as high purity Germanium which has a band gap of less than 1 eV. A bigger band gap allows a semiconductor to work at higher temperatures and to produce a signal with less noise. The downside of having a bigger band gap is that the excitation source used to create the electron hole pair requires a higher energy which lowers the overall efficiency of the system. However, CZT has the ability to operate at room temperature unlike Silicone and Germanium semiconductors which require liquid nitrogen cooling [1].



**Figure 1: CZT samples Detectors 6 and 8 used in characterization analysis**

## 2.2 GROWTH METHODS

The CZT crystals are grown using the travelling heater method (THM). This method of crystal growth offers various advantages over the traditional methods of low or high pressure Bridgman and physical vapour transport. Issues with the traditional methods include polycrystallinity, poor electrical transport properties, inhomogeneity and structural defects [2]. On the other hand, the THM allows for a uniform seeded growth in a chosen  $\langle 111 \rangle$  direction. This method requires a lower growing temperature, is self-purifying and allows for composition control. Downsides to this method include slow growth rates, high temperature gradients [1] and residual Tellurium inclusions left over due to segregation in the cooling process. Te inclusions can lead to undesirable effects such as stray currents and usually need to be broken up by annealing the samples post solidification [17].

## 2.3 USES

CZT crystals are used in gamma and x-ray detection. This is a preferred application for radiation detectors, security screenings and medical imaging. CZT is a suitable detector material for this application because the heavy metals have good stopping power. Low flux applications of 10% CZT include nuclear medicine applications such as cardiac scanning and breast imaging. High flux applications allow for “colour” x-rays which lead to more accurate composition detection such as distinguishing between volatile and domestic liquids during airport security screenings [1].

CZT is completely transparent in the IR (3.5-4.6 % Zn) and its lattice constant can be matched to that of HgCdTe in order to be used as a substrate. CZT is also used for military applications such as night vision goggles and in instruments which can be operated at room temperature in order to avoid heat detection.

## 2.4 ETCHING PROCESS

For part of the X-ray diffraction and photoluminescence analysis, the CZT samples were etched with 2% Bromine Methanol. This type of etch is used because it doesn't change the stoichiometric composition of the surface and it removes oxidation from

the sample. The etching process involved: (1) rinsing in methanol, (2) soaking in 2% Bromine Methanol for 2-8min, (3) double methanol rinse and (4) drying off with a nitrogen gun and vacuum packing. The samples require vacuum packing because they will begin to oxidize again once in contact with the air. Oxidization occurs in 100-200 min depending on the humidity of the storage area [19].

### 3 HIGH RESOLUTION X-RAY DIFFRACTION

#### 3.1 THEORY

##### 3.1.1 X-RAY DIFFRACTION AND THE BRAGG CONDITION

X-ray diffraction is a method of analysing the crystal structure of a material. X-rays are emitted toward and material and radiation scatters as a result of interaction with the atoms. The constructive interference of the wave front, as per Huygen's principle, is known as diffraction. This waveform carries information about the crystal structure and defects of the material [3].

Furthermore, Bragg's law relates the diffraction pattern to the distances of the objects. The incident rays, seen as A and A' in Figure 2, are reflected at the same  $\theta$  at which they enter the material, seen as C and C', and the constructive interference of the rays is examined.

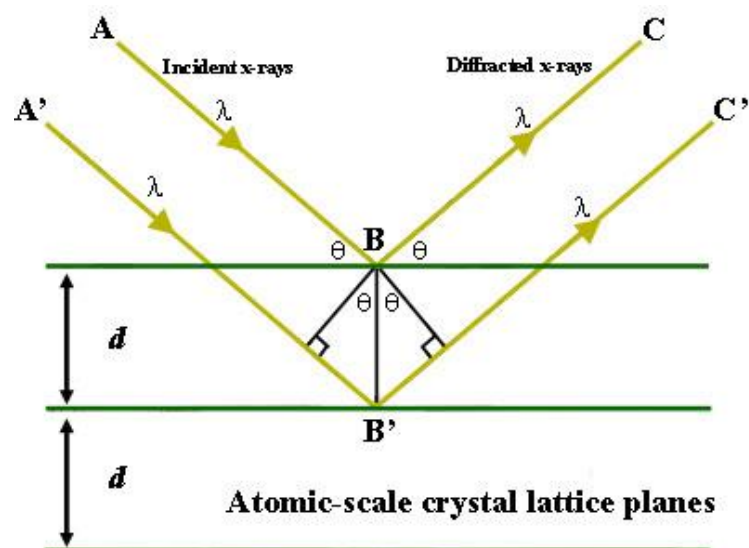


Figure 2: Bragg's law definition [4]

Constructive interference of these beams occurs only when the beam path is equal to an integer number of wavelengths, so that the reflected beams have a similar phase. Bragg's law is shown in Equation 1.

$$2d \sin \theta = n\lambda \quad \text{Equation 1}$$

Bragg's law relates the diffraction angle to the spacing between the objects and shows that there is a reciprocal relation between the two. Larger spacing between the objects results in lower diffraction angles which are used to gauge the distance between atoms in the lattice. As a result, changing  $\theta$  will result in different peaks with different angles that characterize the features of the crystal structure.

### 3.1.2 HRXRD EXPERIMENT SETUP

The high resolution x-ray diffraction measurements were performed using the Bruker D8 Discover Diffractometer seen in Figure 3.



**Figure 3: Bruker D8 Discover diffractometer system analyzing a CZT sample**

The X-ray is emitted from a copper source at a wavelength of 1.54056 angstroms. The sample is mounted onto the holding plate using vacuum suction provided by the machine. The Bruker system has a capability of aligning 5 axes of rotation (x, y, z, phi

and  $\chi$ ) and allows for movements as small as 0.001 degrees. The system is equipped with two detectors. The variable optic detector provides a lower resolution with a highest intensity and the Ge220 analyser crystal provides a higher resolution with a lower intensity. The Ge220 analyser crystal option was used for analysis of all samples.

### 3.1.2.1 BEAM OPTICS: GE220 ANALYZER CRYSTAL

The Ge220 analyser crystal is made from a very high quality Germanium. This crystal is used to narrow down the Bragg diffraction peak. The system set up is seen below in Figure 4.

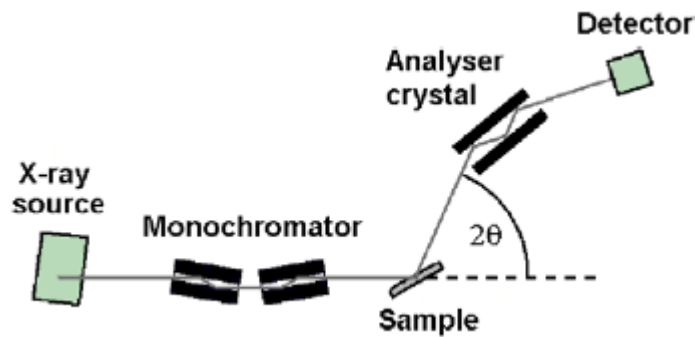


**Figure 4: XRD beam optics set up showing analyzer crystal as part of the machine configuration [11]**

As the signal is reflected from a low to average crystal quality sample, it passes into the analyzer crystal. There the signal is Bragg reflected several times within the crystal which leads to narrowing of the Bragg peak. This is the standard optical set up for high resolution X-ray diffraction work.

### 3.1.3 DETERMINATION OF ZINC CONCENTRATION

From XRD graphs, the lattice constant for each sample can be calculated using Bragg's Law as shown in Equation 1 with a known XRD copper source wavelength of  $\lambda = 0.154051$  nm.

$$2d_{111}\sin\theta_B = n\lambda \quad \text{Equation 2}$$

Employing the geometric properties of a cubic crystal structure, the lattice constant for each sample can be calculated as shown in Equation 3.

$$d_{111} = \frac{a}{\sqrt{h^2 + k^2 + l^2}} \quad \text{Equation 3}$$

The Zinc % concentration can be calculated using Vegard's Law which is a form of linear interpolation. Vegard's Law is shown in Equation 4.

$$a_{CZT} = xa_{ZTe} + (1 - x)a_{CdTe} \quad \text{Equation 4}$$

The accepted values for  $a_{ZTe}$  and  $a_{CdTe}$  are 0.6104 nm and 0.6481 nm, respectively [5].

### 3.2 XRD MEASUREMENTS – 10% REDLEN MATERIAL

#### 3.2.1 DATA FROM REDLEN TECHNOLOGIES

Data on Detectors 6, 8 and Sample 1527-9 were obtained from Redlen Technologies. The data is summarized in Table 1.

**Table 1: Sample information from Redlen Technologies [19]**

Sample	Strain Estimate	EPD/cm <sup>2</sup>	Resistivity	Expected FWHM
Detector 6	1.4	1 x 10 <sup>4</sup>	Low	20-30 arc sec
Detector 8	1.8	8 x 10 <sup>4</sup>	High	60 arc sec
Sample 1527-9	0.7	3 x 10 <sup>4</sup>	Unknown	20-30 arc sec

Redlen Technologies estimated the expected FWHM was based on EPD values [9]. The referenced used is included in Appendix A.

#### 3.2.2 NON-ETCHED SAMPLES ANALYSIS

XRD analysis was performed on Detectors 6 and 8 and Samples 1218-3 and 1527-9. The detector with the Ge220 analyzer crystal was used. The values from the analysis are summarized in Table 2.

**Table 2: Measured and calculated values for non-etched samples using data from XRD**

<b>Sample</b>	<b>Detector 6</b>	<b>Detector 8</b>	<b>1218-3</b>	<b>1527-9</b>
Peak location (2 $\theta$ )	23.8969	23.8969	23.8953	23.8893
Lattice constant (nm)	0.6444	0.6444	0.64499	0.64515
Zinc Concentration (%)	9.81	9.81	8.83	8.43
FWHM (arc seconds)	61.87	59.74	61.00	60.00

The Zinc % concentrations found through the XRD analysis agree with the approximate 9-10 % expected concentration indicated by Redlen Technologies. The data plots are shown in Appendix B.

### 3.2.3 ETCHED SAMPLES ANALYSIS

XRD analysis was performed on Detector 6, Detector 8 and Samples 1218-3 and 1527-9 after etching with 2% Bromine Methanol for 2 minutes. The detector with the Ge220 analyzer crystal was used. The values from the analysis are summarized in Table 3. The graphs are shown in Appendix C.

**Table 3: Measured and calculated values for etched samples using data from XRD**

<b>Sample</b>	<b>Detector 6</b>	<b>Detector 8</b>	<b>1218-3</b>	<b>1527-9</b>
Peak location (2 $\theta$ )	23.8993	23.8869	23.8945	23.8331
Lattice constant (nm)	0.6443	0.6447	0.6445	0.6461
Zinc Concentration (%)	9.73	9.02	9.55	5.30
FWHM (arc seconds)	62.8909	74.7962	61.4756	62.1101

The rocking curve scan for sample 1218-3 showed an interesting result with a double peak pictured in Figure 5.

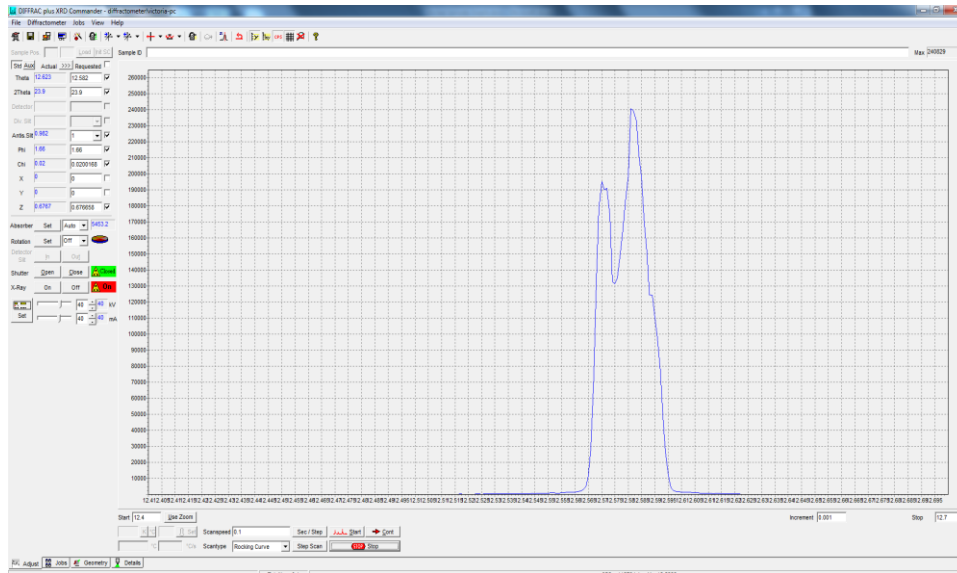


**Figure 5: Double peak seen in XRD rocking curve scan of sample 1218-3**

The double peak could be an indication of a defect in the crystal caused by phase segregation [8]. The X-ray beam hits different locations of the sample depending on the mounting position; therefore, during this scan the beam was located on a defect area.

**3.3 XRD MEASUREMENTS – 4% UVIC CRYSTAL GROWTH MATERIAL**

**3.3.1 EFFECT ON XRD LINE WIDTH WITH ETCHING**

A study on the effect of XRD line width with etching time was investigated. The same sample, Crystal 3, was etched with 2% Bromine Methanol and chemically and mechanically polished for 5 and 8 minutes. The results are shown below in Table 4.

**Table 4: Values of FWHM after different time intervals of etching**

Sample	5 min	8 min
Crystal 3	59.27 arc sec	56.34 arc sec

As seen in Table 4, there was an improvement in the results.

### 3.3.2 XRD FWHM VALUES WITH $2\theta$ - $\omega$ AND $\omega$ - $2\theta$ SCANS

Crystal 4 was analyzed using XRD in order to investigate the FWHM which was used as an indicator for crystal quality. Two scans ( $2\theta$ - $\omega$  and  $\omega$ - $2\theta$ ) were performed using the same settings. The two scans are shown next in Figures 6 and 7.

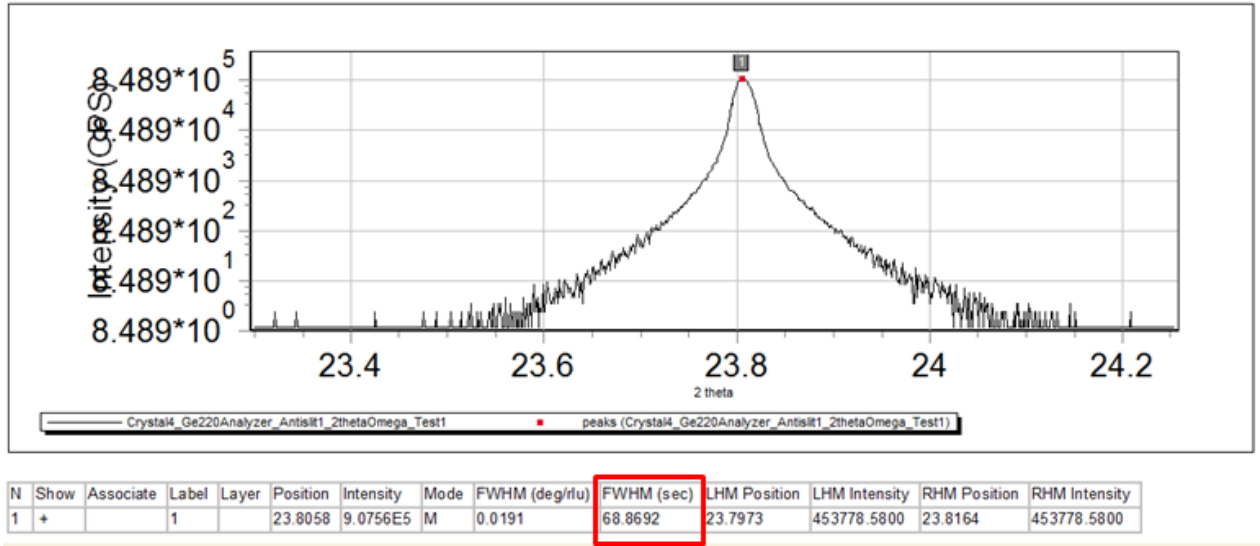


Figure 6: FWHM of 68.8692 arc seconds obtained with  $2\theta$ - $\omega$  scan

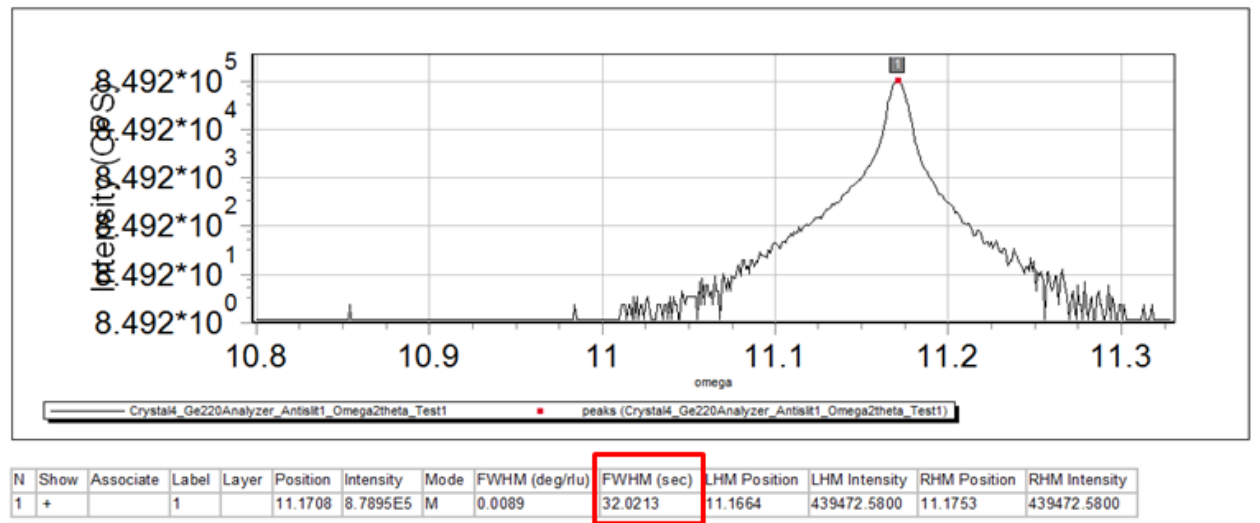


Figure 7: FWHM of 32.0213 arc seconds obtained with  $\omega$ - $2\theta$  scan

The first scan resulted in a FWHM of 68.8692 arc seconds using the  $\omega$ - $2\theta$  method, and a  $\omega$ - $2\theta$  scan resulted in a FWHM of 32.0213 arc seconds. The  $2\theta$ - $\omega$  scan represents the sample being rotated by  $\omega$  and the detector being rotated by  $2\theta$  with an angular ratio of

1:2. In reciprocal space,  $S$  (scattering vector) moves outward from the origin. The length of  $S$  also changes, but the direction stays the same and depends on the offset. The angle with the sample is  $\omega$  and the angle with the crystal lattice is  $\theta$ . This concept is illustrated in Figure 8.

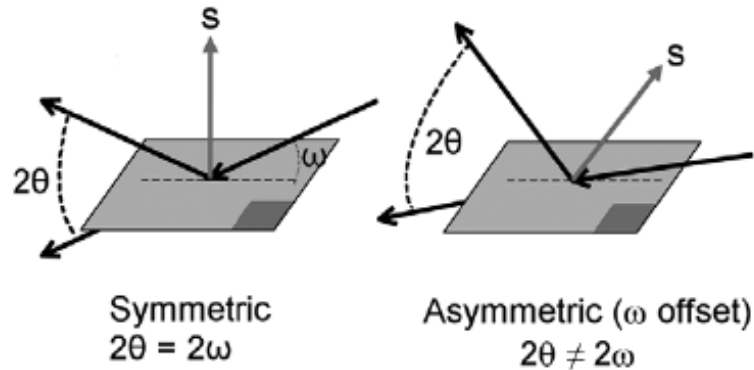


Figure 8:  $\omega$  offset concept in reciprocal space [11]

A  $\omega$ - $2\theta$  is the same as a  $2\theta$ - $\omega$  scan, except that the x-axis is in increments of  $\omega$  and in the second scan it is in increments of  $2\theta$ , respectively. When there is no offset and  $\omega = \theta$ , this is known as a symmetrical scan which is vertical in reciprocal space [11].

## 4 PHOTOLUMINESCENCE

### 4.1 THEORY

Photoluminescence occurs when a system is excited to a higher energy level by absorbing a photon. Then the system spontaneously decays to a lower energy level, emitting a photon in the process [6]. Figure 9 shows a schematic of the process.

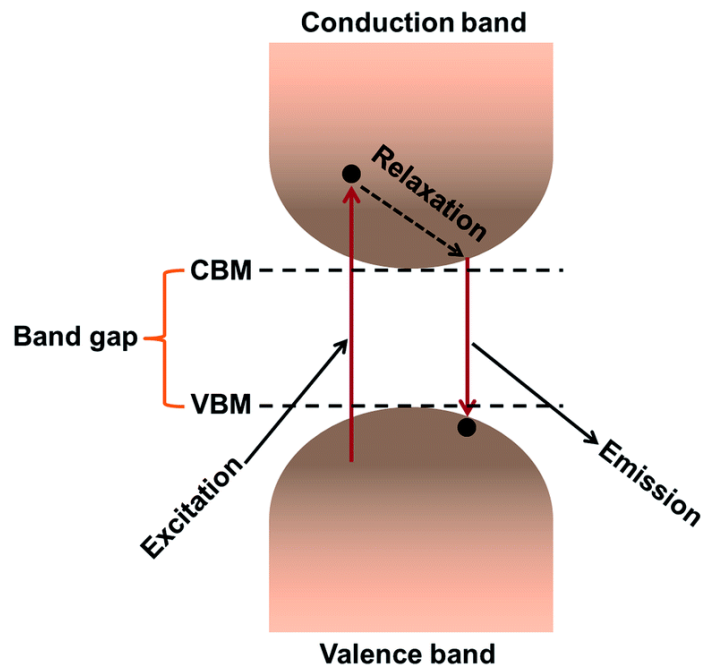


**Figure 9: Process flow diagram for exciting an electron in the conduction band and triggering a photon used to study the material in the electron/hole recombination process [12]**

In order to excite an electron into the conduction band, the material is excited with a monochromatic light beam; however, the excitation source must have a higher energy than the band gap. The absorbed photon leads to an electron which is excited into the conduction band leaving behind a hole in the valence band. As the excited electron moves to a lower energy in the conduction band it can release some stored energy as a phonon [6]. When the excited electron recombines with the hole in the valence band, the stored energy is released as a photon. This photon can be collected and studied. The emitted photon has a unique energy signature which carries information about the structure, defects and impurities of the material [6].

#### 4.2 PHOTOLUMINESCENCE EXPERIMENTAL SETUP

The photoluminescence setup has three parts: optical setup (lenses, filter and fibre), monochromator, and a Nitrogen cooled InGaAs array detector (which is connected to a computer).

### 4.2.1 OPTICAL SETUP

The PL set up used in the lab was comprised of two optical lenses as seen in Figure 10. The first lens (lens 1) has a focal point of 4.5 cm and is used to pick up the PL from the sample which is excited by a 532 nm green laser (Model 7950-L104). The sample is brought into focus by adjusting the stage seen below lens 1.

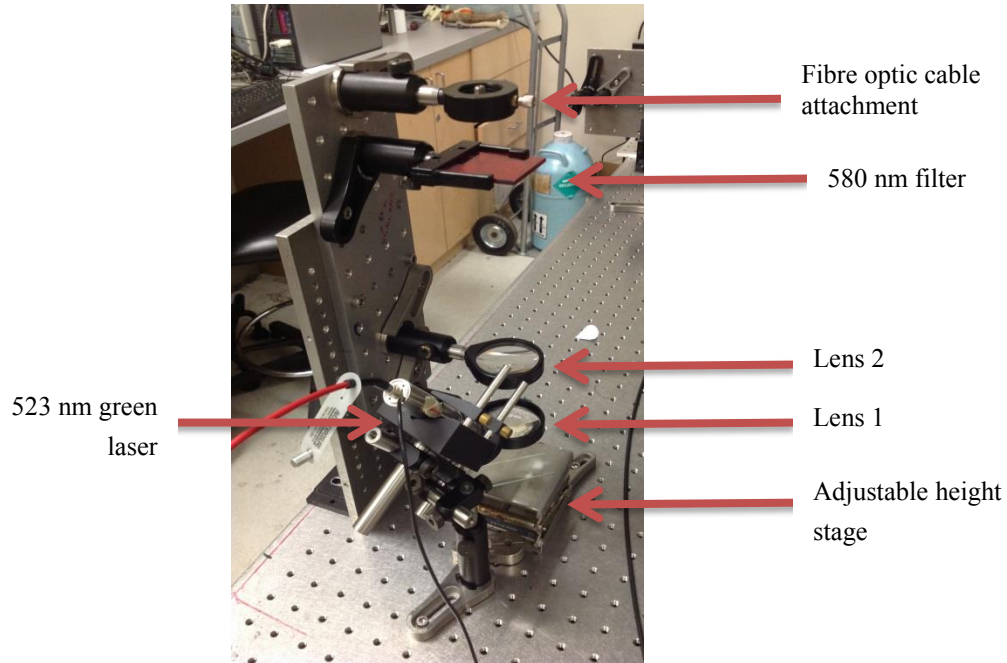


**Figure 10: Photoluminescence set up used for experiment**

Lens 1 collimates the signal into lens 2 which is positioned ~5 cm above. The placement of the second lens with respect to the first one is less important because the PL enters the lens in a column. The second lens has a focal point of 19.5 cm and is placed at this distance from the fibre optic cable inlet.

The signal going into the fibre optic cable is filtered by using a 580 nm red colour filter from Thorlabs. The location of this filter with respect to the rest of the setup is of lower importance but it is good to place it closer to the fibre optic cable opening such that the laser signal and room lights are attenuated. It is desirable to filter the laser in order to avoid saturation of the detector.

The fibre optic stand is equipped with two nobs which allow for adjustment in the x and y axis directions. This allows the fibre optic cable opening to be aligned directly into the focal point of lens 2 such that the maximum signal is picked up and sent to the monochromator. The monochromator and the fibre optic cable must have the same numerical aperture. This is dimensionless number which measures the range of angles over which a system can accept or emit light. Figure 11 illustrates the concept of acceptance angles.

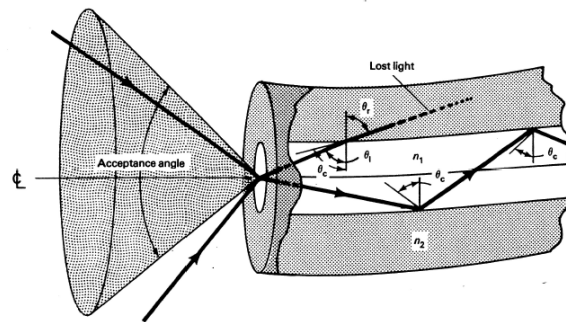


**Figure 11: Range of acceptance angles in a fiber optic cable required to undergo internal reflection and transmit a signal**

#### 4.2.1.1 MONOCHROMATER

The monochromator works by accepting light from a fibre optic cable. The light is reflected by a mirror and onto the diffraction grating. The grating splits the light into different wavelengths. Tilting the grating leads to satisfying Bragg conditions at different wavelengths and this allows for a selection of which wavelength can be put out to the detector array. Figure 12 shows a typical monochromator set up.

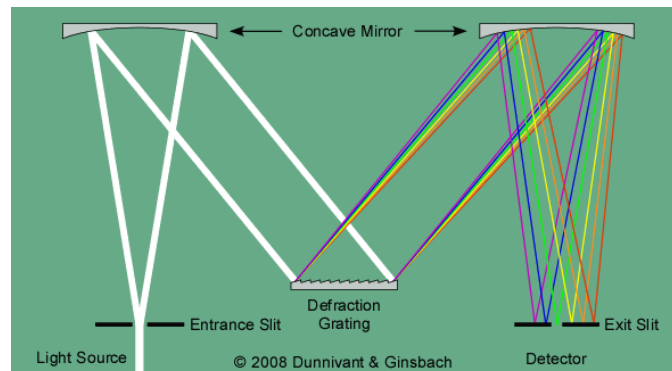


**Figure 12: Typical monochromator set up showing how light is split into different wavelengths using a diffraction grating [14]**

In the case of CZT, the diffraction grating is chosen to be at 800 nm which matches the wavelength of the PL peak.

#### 4.2.1.2 INGAAS DETECTOR ARRAY

After the desired wavelength has been selected, the signal is sent to the InGaAs detector array (Roper Scientific Model 7410-0003). In order to lower the thermal noise, the detector is cooled down to  $-105^{\circ}\text{C}$  by pouring  $\text{LN}_2$  into the holder connected to the detector array. The InGaAs material in the detector is grown on an InP substrate. The band gap of InP at  $-105^{\circ}\text{C}$  is around 892 nm (1.39 eV), which appears like a kink in the PL measurements [15]. To remove the kink, the PL spectrum should be normalised to the throughput of the optical setup. The measurements for this experiment were not normalized because they were performed at room temperature when the PL which has a sharp peak and the kink is not seen in the spectra.

### 4.3 PHOTOLUMINESCENCE MEASUREMENTS

#### 4.3.1 NON-ETCHED SAMPLES ANALYSIS

Photoluminescence measurements were performed for both Detector 6 and 8 and samples 1218-3, 1529-9, 2964-11, and 3495-4. Each of the samples was excited using a 523 nm green laser and tested at exposure times of 10, 30 and 60 second intervals. The data from the detector was exported to MS Excel and plotted. Figure 13 shows the results for intensity vs. wavelength for a 10 second exposure of all samples.

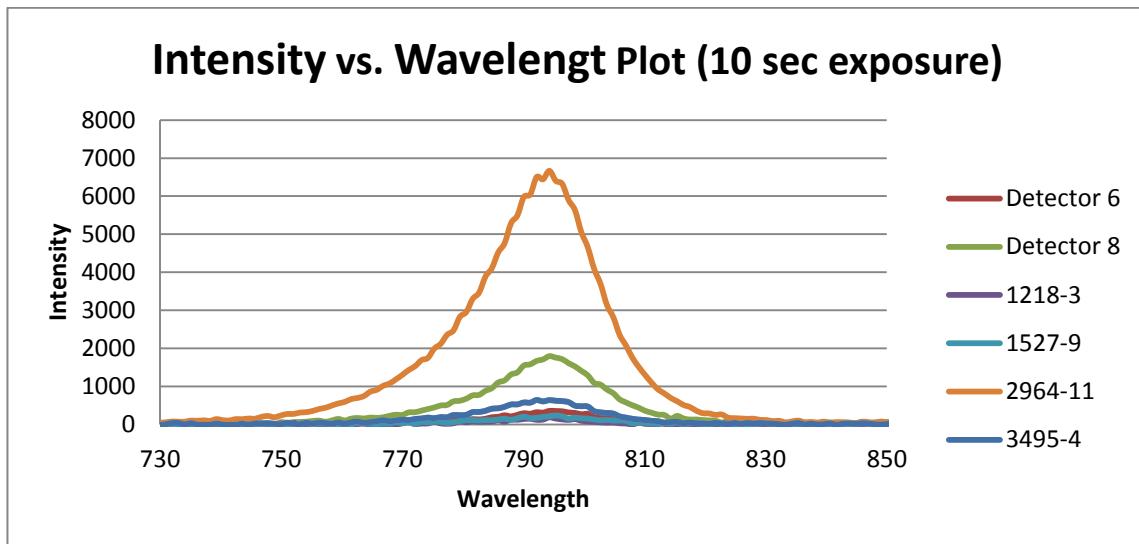


Figure 13: Intensity vs. Wavelength PL plot for a 10 second exposure time

As can be seen by the figure, 2964-11 appears to have the most PL and sample 1218-3 having the least PL.

A comparison plot for Energy vs. Intensity<sub>1</sub> was also made. The wavelength and intensity spectrums were converted to Intensity<sub>2</sub> by the relationship shown in Equation 5.

$$E = h\omega = \frac{hc}{\lambda} \quad \text{Equation 5}$$

The values which need to be related are shown in in Equation 6.

$$I_1 d\lambda = I_2 dE \quad \text{Equation 6}$$

The derivative of Equation 5 is shown in Equation 7.

$$dE = \frac{hc}{\lambda^2} d\lambda \quad \text{Equation 7}$$

Substitution of Equation 7 into Equation 6 is shown in Equation 8.

$$I_1 d\lambda = I_2 \frac{c}{\lambda^2} d\lambda \quad \text{Equation 8}$$

From this, the relationship between Intensity<sub>1</sub> as a function of wavelength and Intensity<sub>2</sub> as a function of energy can be derived (Equation 9).

$$I_2 = \frac{I_1 \lambda^2}{hc}$$

Equation 9

Figure 14 shows the resultant plot for Energy vs. Intensity for a 10 second exposure time.

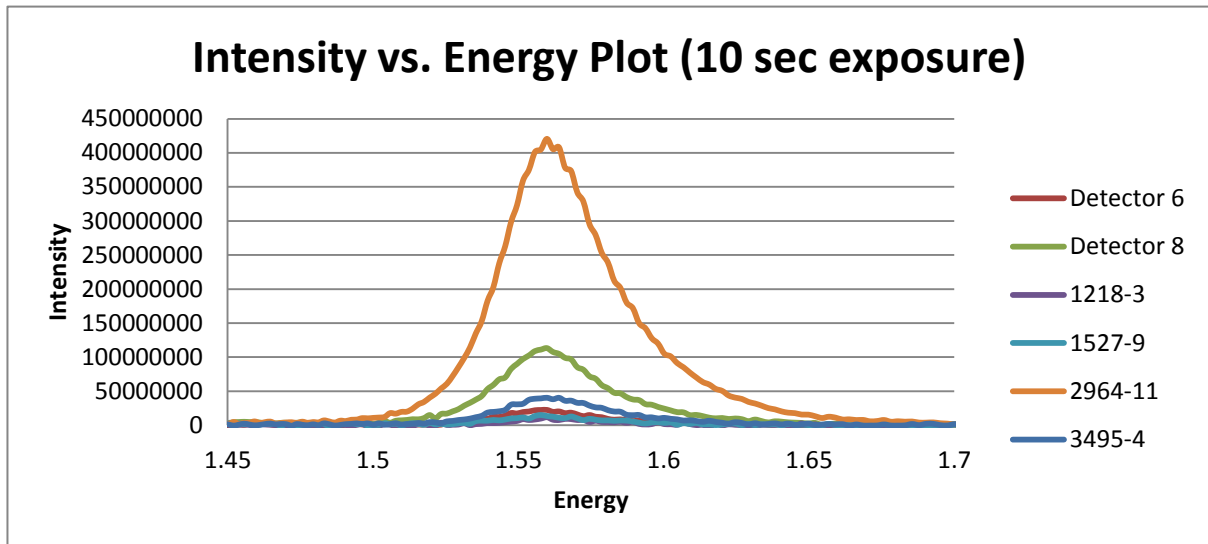


Figure 14: Intensity vs. Energy plot for CZT samples at a 10 second exposure time

As seen with the intensity vs. wavelength plots, sample 2964-11 showed the highest intensity and 1218-3 the least.

#### 4.3.2 ETCHED SAMPLE ANALYSIS

The samples were etched with a 2% Bromine Methanol solution at Redlen Technologies and were vacuum packed in order to avoid oxidation and to be examined at UVic. The samples were analysed at a 1 second and a 10 second exposure time. Figures 15 and 16 show the results from the 1 and 10 second exposure times, respectively.

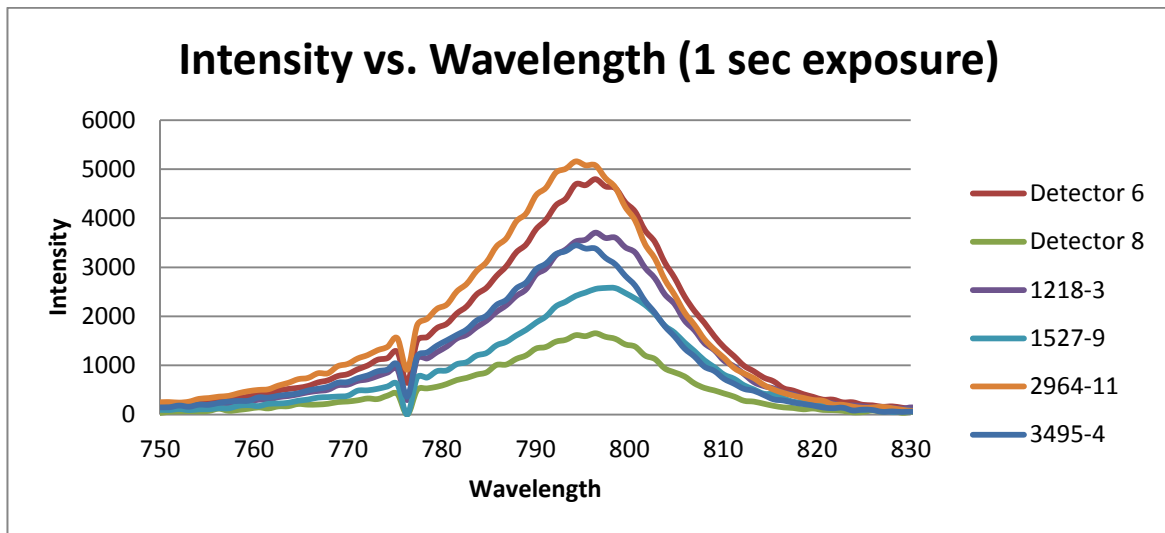


Figure 15: Etched samples PL data intensity vs. wavelength plot (1 second exposure)

The uniform drop of the signal shown at approximately 775 nm is a result of a dead pixel in the detector array.

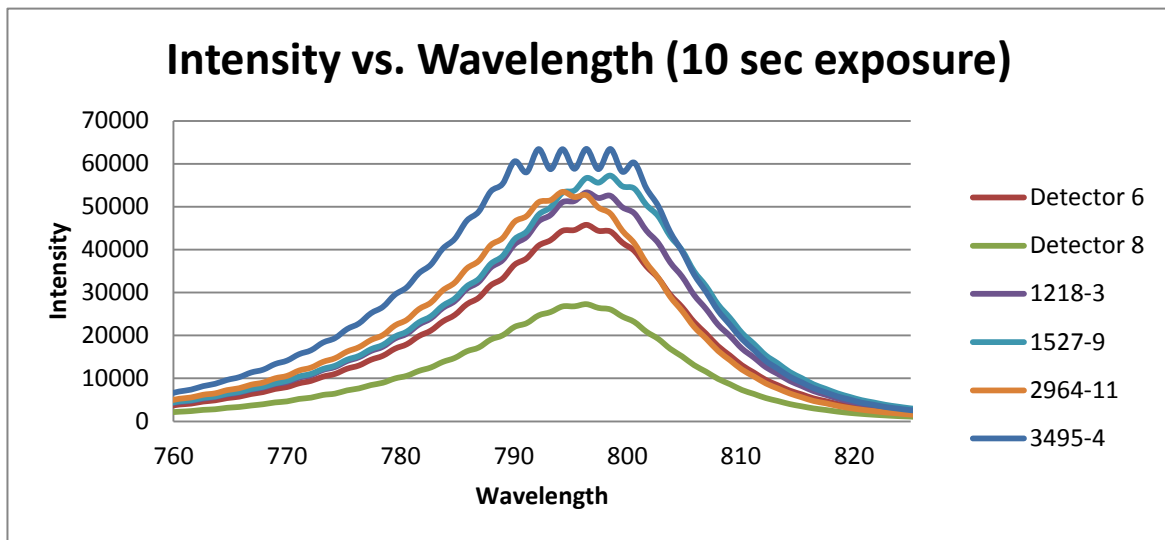


Figure 16: Etched samples PL intensity vs. wavelength plot (10 second exposure)

The non-uniform rippling peak observed with sample 3495-4 is a result of saturation of the detector. The maximum intensity before saturation is 60,000 counts.

As discussed in Section 4.3.1 and using the relationship derived in Equation 9, the corresponding Intensity vs. Energy plots for the samples were obtained. They are shown next in Figures 17 and 18.

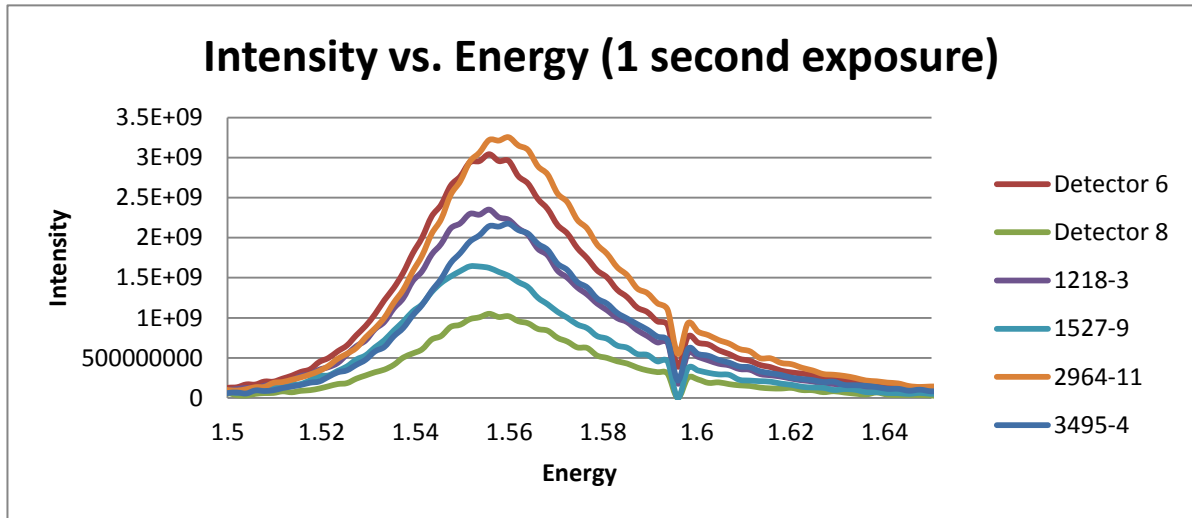


Figure 17: Etched samples Intensity vs. Energy plot (1 second exposure)

The uniform drop seen on the signals around 1.60 eV is the same dead pixel seen in Figure 15.

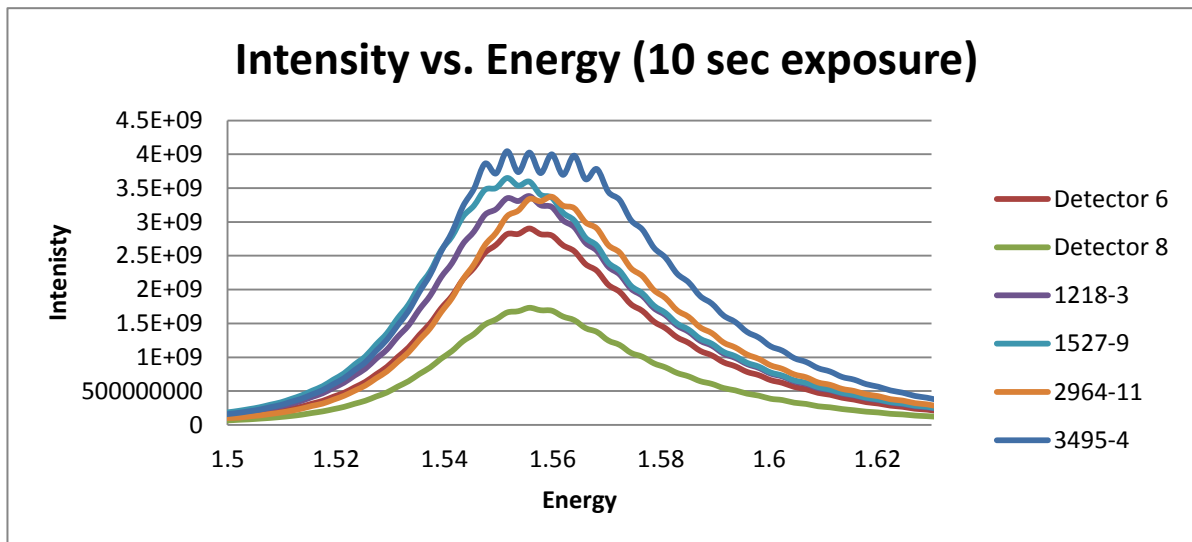


Figure 18: Etched samples Intensity vs. Energy plot (10 second exposure)

As discussed with Figure 16, the PL from 3495-4 exceeded the saturation limit of the detector and resulted in a non-uniform peak.

#### 4.4 ZINC CONCENTRATION

The Zinc concentration in the CZT crystals can be determined by calculating the band gap energy. The band gap energy is related to the wavelength at which the peak of the photoluminescence is observed. Equation 10 is used to find the band gap energy.

$$E_g = \frac{hc}{\lambda} \quad \text{Equation 10}$$

This gives a result in Joules which needs to be converted to eV by the relation:

$$1\text{eV} = 1.6 \times 10^{-19} \text{ J}$$

The Zinc concentration can be found from various predictive models. The model which was used here is described by Equation 11 [7].

$$E_g = 1.510 + 0.606x + 0.139x^2 \quad \text{Equation 11}$$

The predictive model was developed based on curve fitting experimental data. The model uses a second order polynomial, because using higher order polynomials can be inaccurate due to an oscillatory behaviour known as the Runge Phenomenon. The band gap energies and correlated Zinc molar concentrations are shown in Table 5.

**Table 5: Zinc concentration estimation from PL analysis**

	<b>Detector 6</b>	<b>Detector 8</b>	<b>1218-3</b>	<b>1527-9</b>	<b>2964-11</b>	<b>3495-4</b>
Wavelength (nm)	797.0	796.5	797.8	798.5	795.5	796.0
Band gap Energy (eV)	1.558	1.559	1.556	1.555	1.561	1.560
% Zinc	7.73	7.89	7.49	7.27	8.21	8.05

## 5 SCANNING ELECTRON MICROSCOPY

### 5.1 THEORY

Scanning Electron Microscopy (SEM) is a method both magnified image generation and of chemical analysis.

#### 5.1.1 SCANNING ELECTRON MICROSCOPE SETUP

A diagram of a typical SEM set up is shown next in Figure 19. In electron beam is generated by heating a tungsten filament and applying a potential through an anode which pulls individual electrons from the filament. The anode accelerates the divergent electron beam down the microscope column. The column must be kept at a high vacuum in order to maximize the mean free path of the electrons. In order to converge and focus the beam, it passes through a condenser electromagnetic lens. Next, the deflection coils allow for movement of the beam to different locations on the sample since an image is generated as the beam rasters over the sample.

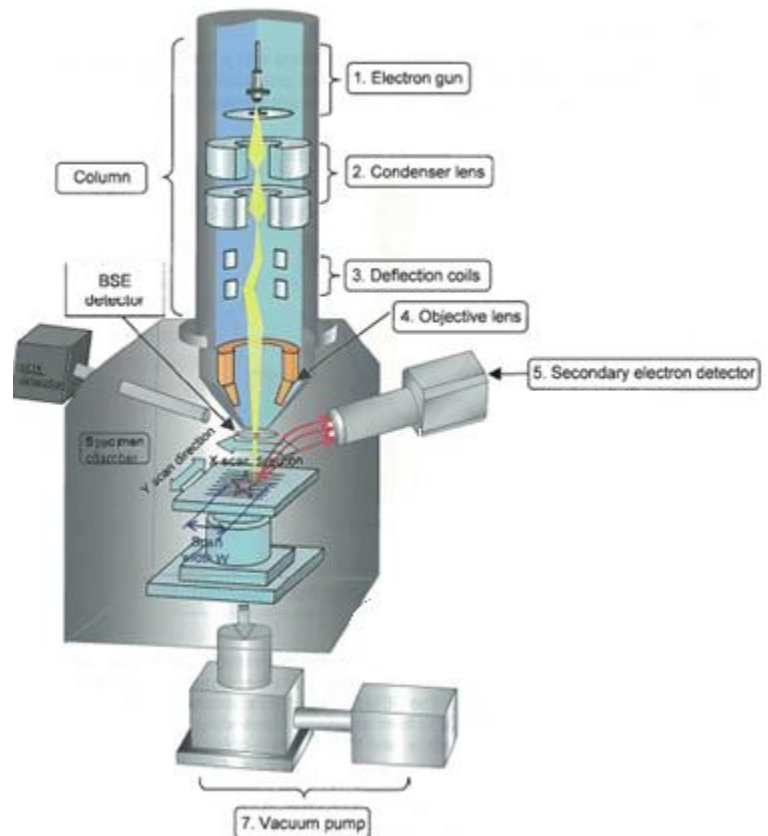


**Figure 19: Scanning Electron Microscope internal diagram [16]**

The objective lens further focuses the beam before it irradiates the sample.

By irradiating the sample with the electron beam various signals are generated. These include: secondary electrons, backscattered electrons, elastically and inelastically scattered electrons, characteristic x-rays and cathodeluminescence [16].

### 5.1.2 SCANNING ELECTRON MICROSCOPE IMAGING AND COMPOSITION ANALYSIS

The SEM mainly utilizes secondary electrons to form an image. Secondary electrons are produced near the surface of the sample when the electron beam knocks out inner electrons from atoms in the sample. These knocked out electrons escape the sample and are detected and used to produce a fine topographical image of the surface. As a result of using electrons, a monochromatic image is produced.

The SEM is equipped with an x-ray detector which is used for elemental analysis. When the electrons in the primary beam interact with the specimen, they can knock out an inner electron from a sample atom. This vacancy in a lower energy shell will be filled by an electron in a higher energy orbital by a process known as a transition. During the transition, a characteristic x-ray is emitted which has the same energy as the difference in energy between the two orbitals. The wavelength of the x-ray is characteristic of the atom because each element has different energies between its orbitals. These can be used to determine the materials present in the specimen.

### 5.2 SEM MEASUREMENTS

The analysis was performed on both Detectors 6 and 8 using a Hitachi S-3500N at the University of Victoria. The machine used is shown in Figure 20.

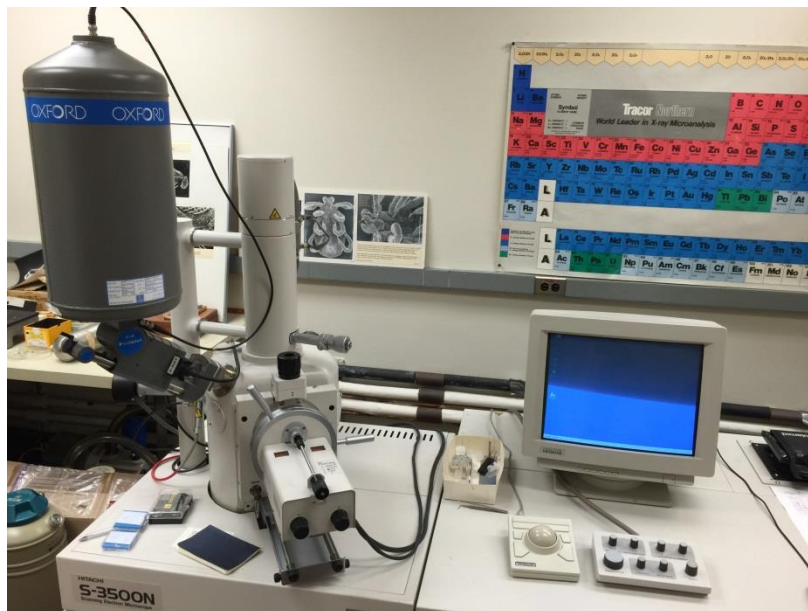
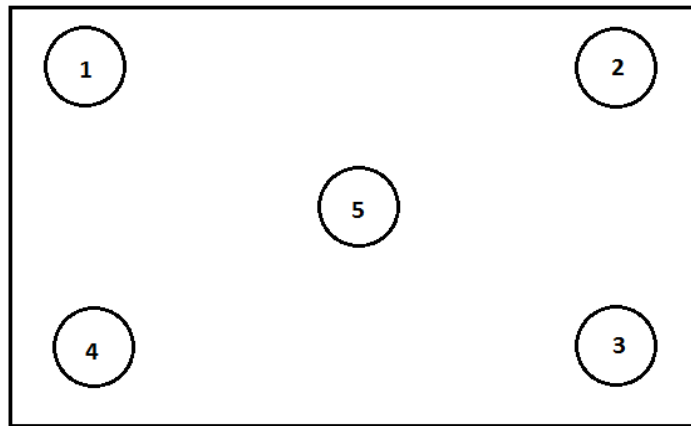


Figure 20: Hitachi S-3500N Scanning Electron Microscope at UVIC

The samples were loaded in the machine and an elemental analysis was performed. Next, images of the surface were taken. These images showed pitting and other surface defects which were used to correlate the surface performance results obtained in the XRD analysis.

### 5.2.1 CHEMICAL COMPOSITION

Detectors 6 and 8 were analyzed at five different locations. The chosen locations are shown in Figure 21.



**Figure 21: Location map of the spots used in SEM analysis of Detectors 6 and 8**

The qualitative chemical composition for both Detectors 6 and 8 was found. Both samples were found to be comprised of only Cd, Zn and Te at all five test locations. A sample spectral analysis for each detector is shown next in Figures 22 and 23.

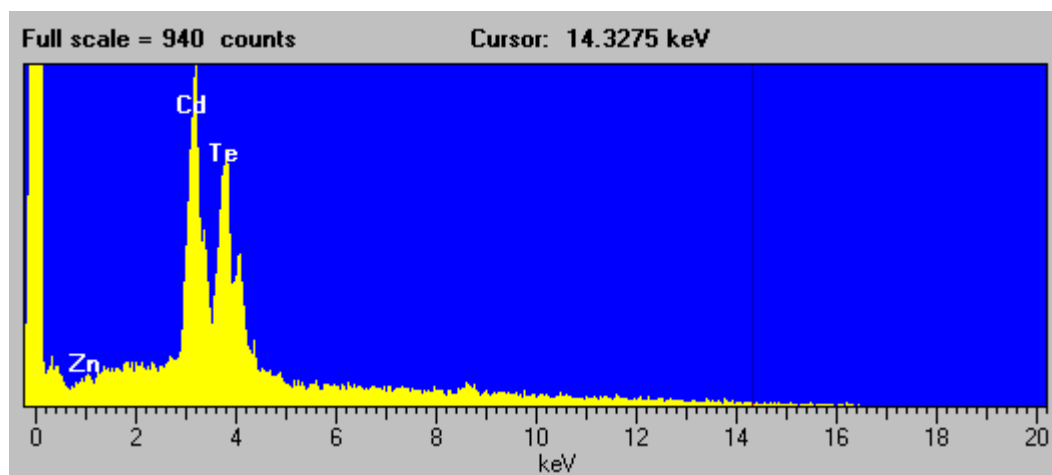


**Figure 22: Qualitative spectral analysis results for Detector 6**

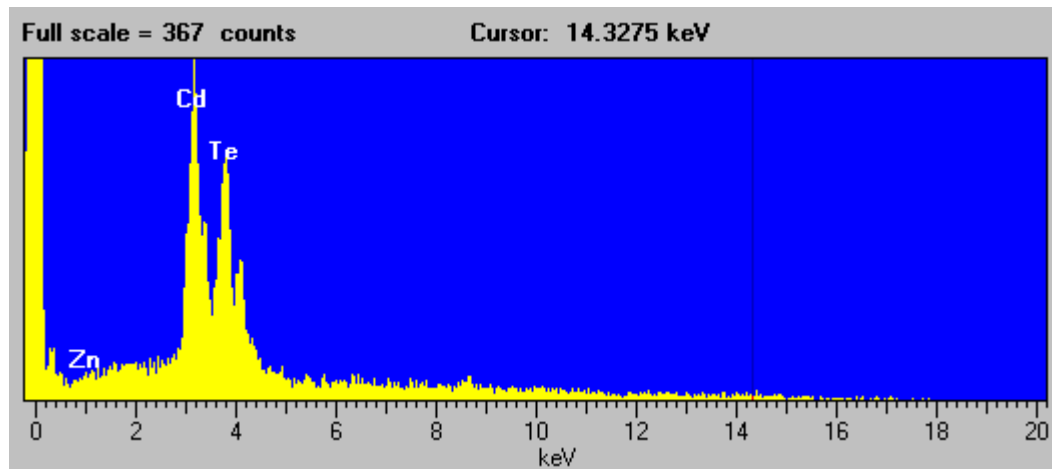


Figure 23: Qualitative spectral analysis results for Detector 8

### 5.2.2 SURFACE PICTURES

Screen captures were made at five locations on each sample. The pictures were taken at a 100x magnification. A lower magnification was chosen because the samples are single crystals and therefore there would be no grain boundaries to observe. The images are shown next in Figures 24 and 25.

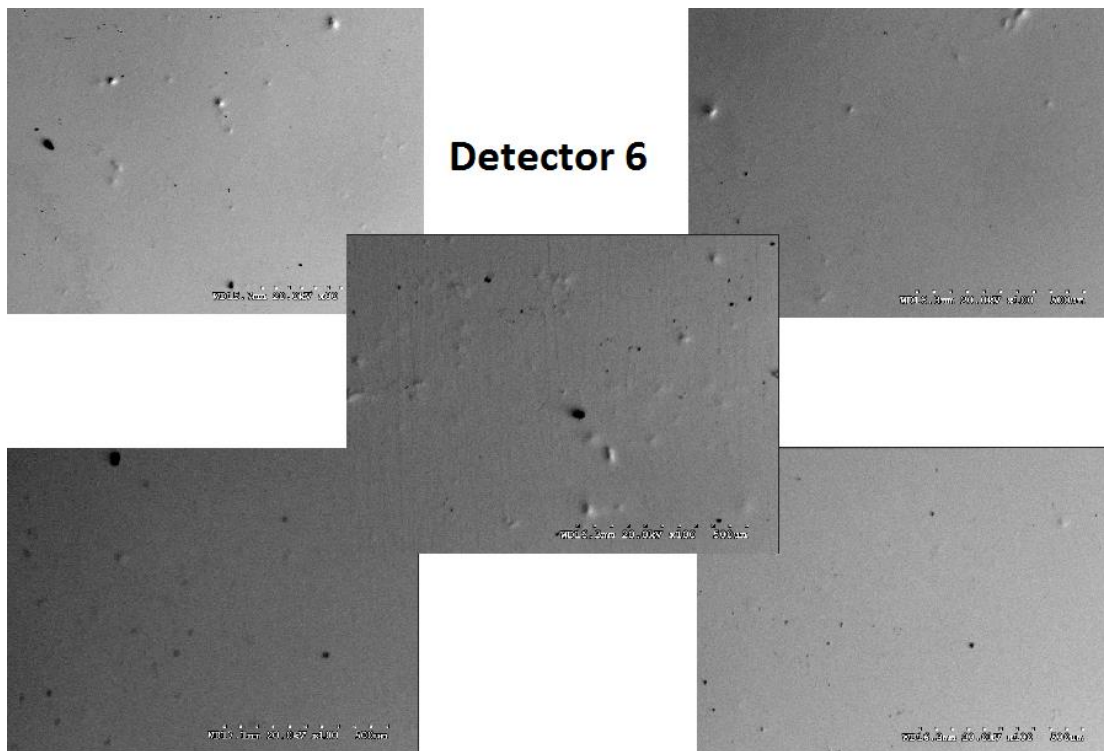


Figure 24: SEM images of Detector 6 at 100x magnification

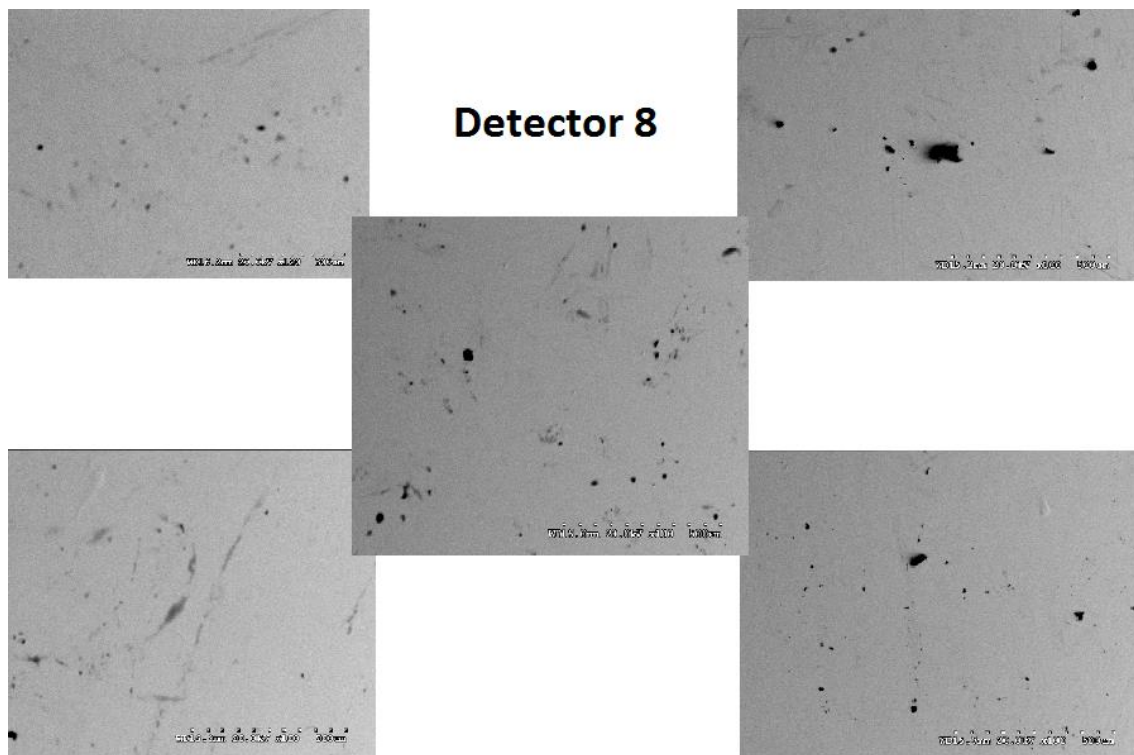


Figure 25: SEM images of Detector 8 100x magnification

## 6 IR TRANSMISSION

### 6.1 THEORY

#### 6.1.1 IMAGING WITH IR TRANSMISSION

IR Transmission is a method of imaging the inside structure of a sample. A thermal light source (Halogen Lamp) is used to produce a spectrum of radiation. This spectrum includes good intensity in the IR range. An IR image is obtained when light is then condensed onto the back side of the sample through a sub-stage condenser. This produces a cone of light suitable for the objective lens of the microscope. The focus and aperture of the condenser are adjusted to the objective lens. This ends up forming two cones of light, one cone from the condenser narrows as it rises to a point, the focal plane, it then diverges into an inverted cone. The wide side of this cone is then incident on the objective lens of the microscope [18].

Using reflected light geometry, the surface can be examined by placing the surface of the sample on the focal plane of the objective lens. If the surface is rough, only a range

of heights will be in focus and some out of focus. The range of focus is known as the depth of field. The stage height can be manually adjusted to bring different height ranges of the sample into focus. There is a focal plane of perfect focus then a range to either side that is the depth of field. Unlike reflection microscopy, the focal plane does not need to be on the surface of the sample to see features. The sample can be moved such that the focal plane is positioned inside the sample. In this way, an image of what is inside the material is obtained [17].

This method of imaging works only if the sample is reasonably transparent to radiation. Areas of high transmittance are bright and of low transmittance are dark. In the case of CZT, the material is relatively transparent in the IR range; however, Te is not transparent in the IR range. Therefore, tellurium inclusions (a well-known material defect) in CZT can be resolved by IR transmission. The inclusions are essentially droplets of pure Te segregated during the solidification process. These appear as black dots of near zero transmittance. Other variations in the material may also become visible, again due to some change in its transmittance [17].

### 6.1.2 IR TRANSMISSION SETUP

The microscope optics are designed to reflect and transmit IR radiation through the use of an IR compatible objective lens. The IR lens (Olympus U-CMAD3 model) and IR camera (MTI VE1000) system is shown in Figure 27.

The light from the objective lens is focused onto the detector of the IR video camera. The IR detector used is a lead sulphide vidicon. This is a CRT that is reading the intensity of an image projected on the detector material (lead sulphide). These were common for all video cameras before CCDs. The CRT scans 700 lines

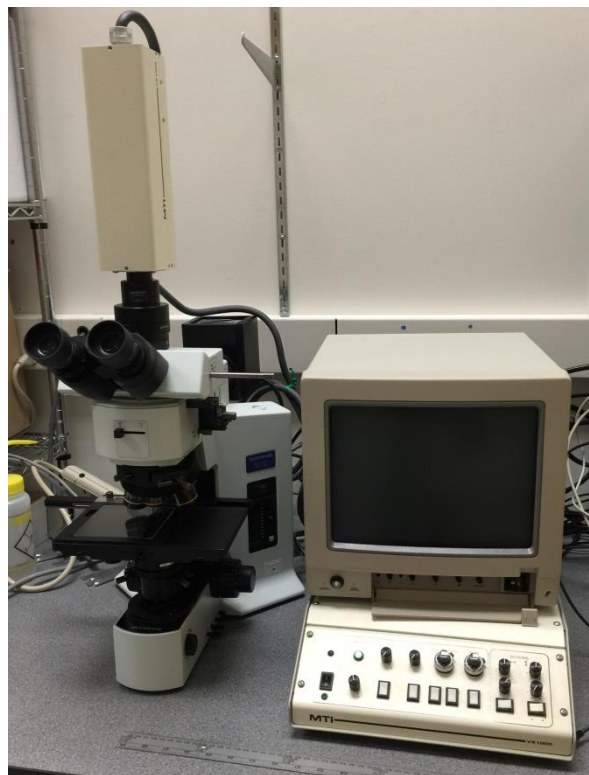


**Figure 26: IR Transmission microscope at UVIC Crystal Growth Lab**

which is what produces the image on the monitor. This is basically an old analog TV setup. The detector is sensitive to light from 400-1800 nm [18]. The frame grabber captures the TV image into digital form. Essentially it is ADC for the analog TV signal to pixelated digital image.

## 6.2 IR TRANSMISSION MEASUREMENTS

IR transmission microscopy was used to image Detectors 6 and 8. This type of analysis method shows dislocations, defects and Te inclusions. These can all be linked to the performance of the device. Figure 28 shows a sample image used for interpretation of the results.

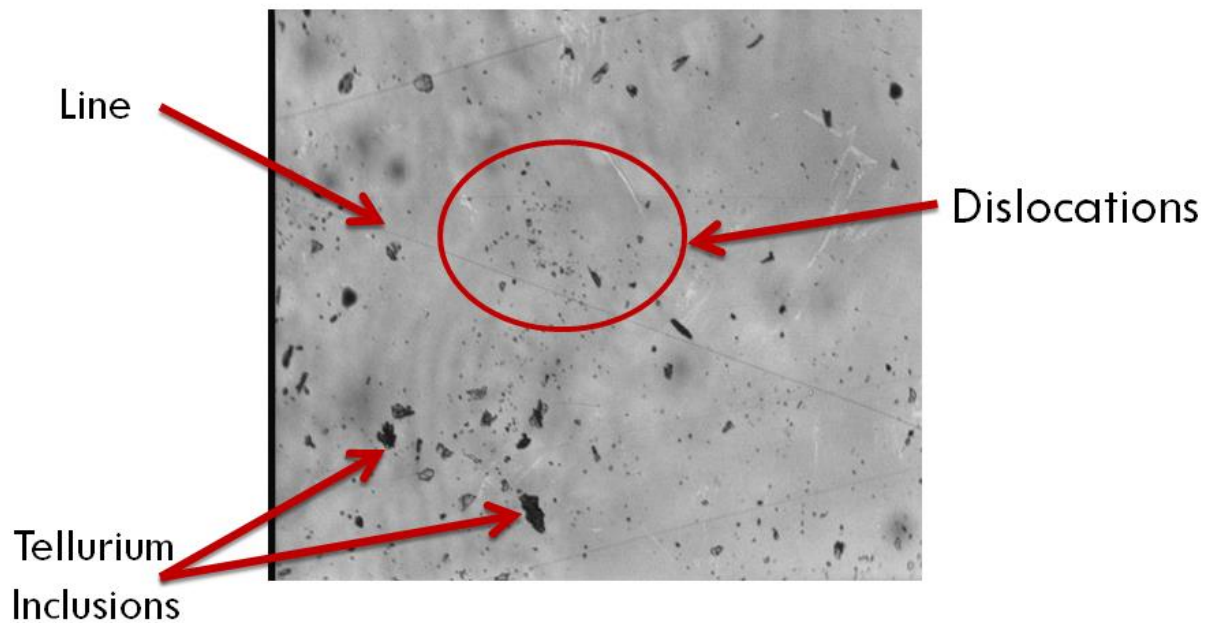


Figure 27: Internal image of Detector 8 showing dislocations and Tellurium inclusions

Images of both Detectors 6 and 8 were taken at the surface, middle and bottom of the samples. Figures 29 and 30 show the internal structures of Detectors 6 and 8.

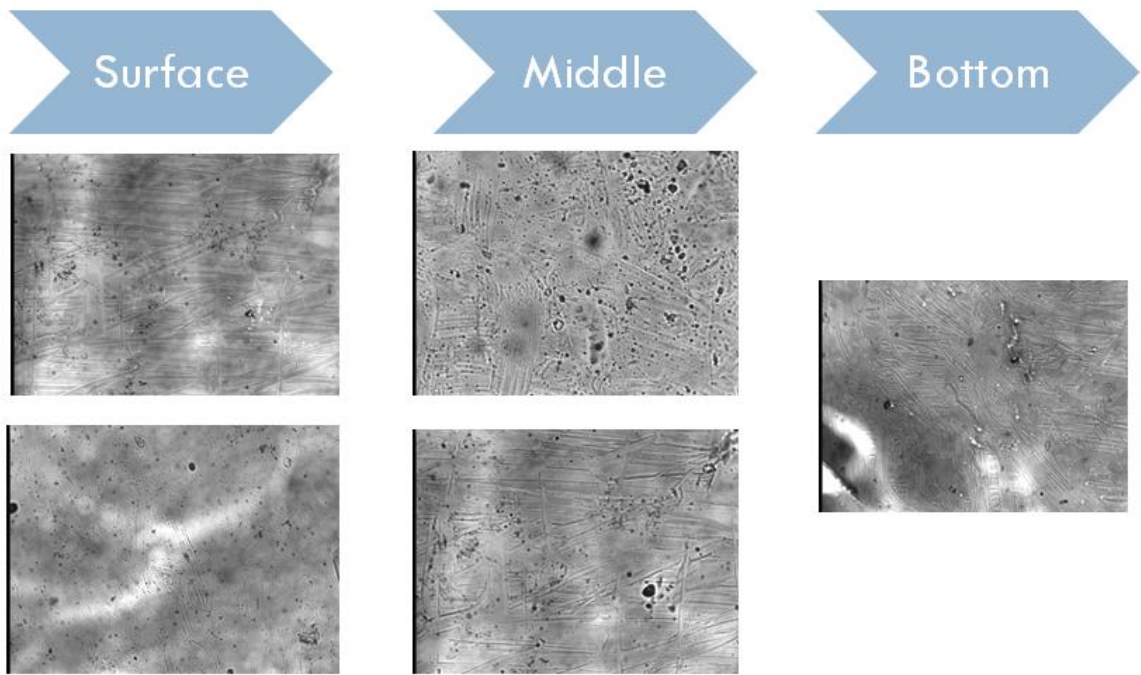


Figure 28: Surface, middle and bottom IR transmission images of Detector 6

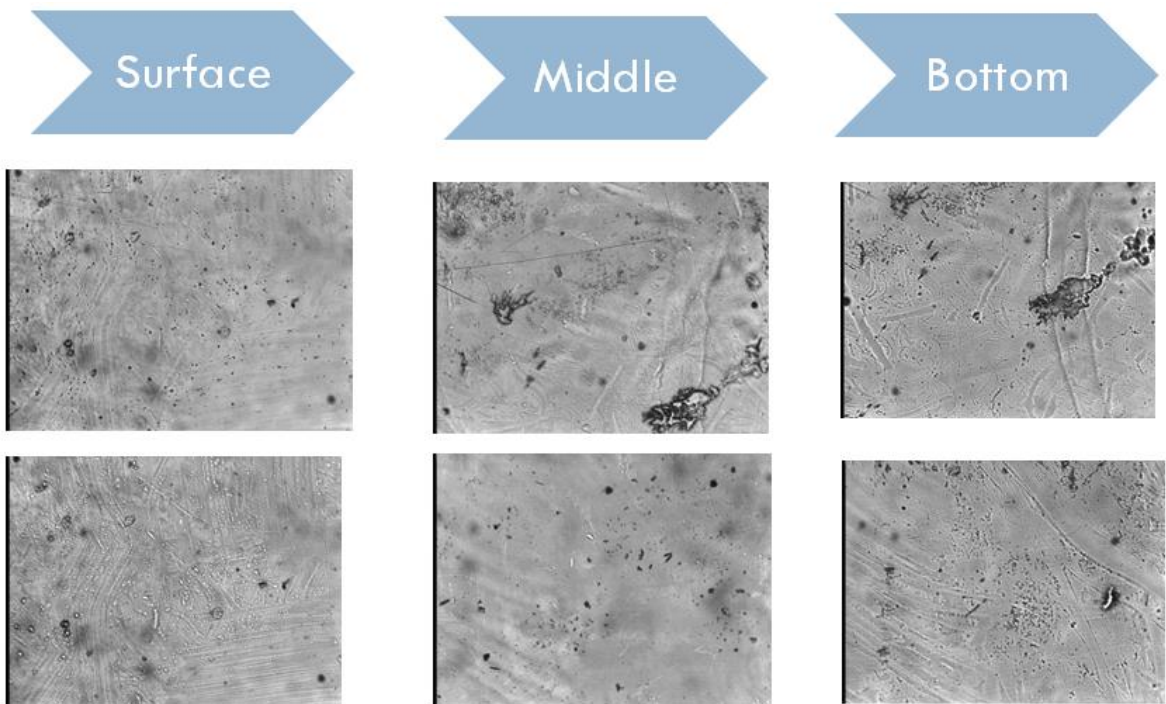


Figure 29: Surface, middle and bottom IR transmission images of Detector 8

## 7 DISCUSSION

### 7.1 ETCHED VS. NON ETCHED RESULTS

#### 7.1.1 X-RAY DIFFRACTION

The XRD line widths between non-etched and etched samples were compared and are shown in Table 6.

**Table 6: Values comparing non-etch and etched FWHM results after 2 min 2% BrMeth etch**

Sample	Non-Etched (arc sec)	Etched (arc sec)	Time (s)
Detector 6	61.87	62.89	2 min
Detector 8	59.73	74.80	2 min
1218-3	61.00	61.48	2 min
1527-9	60.00	62.11	2 min

As can be seen by the values in Table 6, there wasn't an improvement in the XRD line width with etching for 2 minutes. A study from the Department of Physics in Yunnan University, China showed that a combination of aggressive chemical and mechanical polishing in conjunction with etching between 50 minutes and 2.5 hours resulted in a big decrease in the FWHM going from 628 arc seconds to 11 arc seconds [10]. A sample from UVIC Crystal Growth was tested by chemically mechanically polishing and etching for 5 and 8 minutes, respectively. The data is shown in Table 7.

**Table 7: Values comparing FWHM results after different times of 2% BrMeth etching**

Sample	5 min	8 min
Crystal 3	59.27 arc sec	56.34 arc sec

The data in Table 7 showed improvements in the XRD line width from the 5 min to the 8 min etch. The improvement in the line width is a reasonable assessment of the imperfections in the lattice but it has also been found to correlate with the surface of the sample and the measurement conditions. Although there are still defect layers at several  $\mu\text{m}$  below the surface, the surface defects have been removed by polishing and etching

the surface to be mirror-smooth [10]. With this said, the results from the Redlen samples and UVIC Crystal Growth cannot be compared as it is possible one set of samples needed more polishing for a better surface quality which improved the results. However, the results support previous studies that with more polishing and etching, a smaller FWHM width is achieved.

### 7.1.2 PHOTOLUMINESCENCE

As seen in the results in Section 4.3, the PL intensity was improved after etching the samples for 2 min with 2% Bromine Methanol. There was a 10-fold increase in PL intensity between the two sets of data measurements and the intensity increase was observed with all of the samples. The improvement in intensity is a result of removing the oxide layer from the samples which acted as a recombination center for electron hole pairs trapping the PL inside the sample.

It must be noted that the optical system used with the etched samples was better aligned compared to the data showing the non-etched sample's results. The alignment of the system can be determined by seeing the largest intensity count which can be obtained with a highly doped sample of p-GaAs. The maximum count obtained by the system with the non-etched samples was 5,000 counts and with the etched samples it was 12,500 counts. This means that the system was 2.5 times better aligned. This resulted in more of the PL signal being focused into the fibre optic cable inlet. Even with this consideration, the PL intensity after etching was significantly improved.

## 7.2 ZINC CONCENTRATION COMPARISON

The Zinc concentration of the samples was measured by XRD and PL. The results are shown in Table 9.

**Table 8: Zinc concentration comparison between XRD and PL results**

<b>Sample</b>	<b>Detector 6</b>	<b>Detector 8</b>	<b>1218-3</b>	<b>1527-9</b>
% Zinc XRD	9.81	9.81	8.83	8.43
% Zinc PL	7.73	7.89	7.49	7.27
% Difference	21.20	19.57	15.18	13.76

As can be seen by the data in Table 8, the results for the Zinc concentration obtained by XRD and PL analysis agree with an approximate error of 17.4%. It must be noted that some error with the PL Zinc concentration comes from the predictive model which was used [7]. This model was based on a study which curve fitted temperature to known data and used a second order polynomial approximation.

### **7.3 XRD LINE WIDTH AND SURFACE/INTERNAL QUALITY**

#### **7.3.1 SURFACE QUALITY**

A comparison between Detectors 6 and 8 showed that Detector 6 had a narrower line width. The surface quality of the crystals was examined with SEM and this showed that the surface of Detector 8 was in much worse shape. This finding supports the expected results because XRD is a surface characterization method. A study of this thesis showed that more polishing and etching of a sample's surface resulted in a narrower peak, therefore having a rougher surface would account for a wider peak. Furthermore, information provided by Redlen Technologies also predicted, based on an etch pit density (EPD) count [9], that the FWHM of Detector 8 will be bigger. This evidence further supports the experimental FWHM and surface quality observed with SEM.

#### **7.3.2 INTERNAL QUALITY**

IR Transmission results showed that the internal structure of Detector 8 had more irregularities and Te inclusions when compared to Detector 6. This will result in worse results for a FWHM measurement.

## **7.4 PHOTOLUMINESCENCE INTENSITY AND SURFACE/INTERNAL QUALITY**

### **7.4.1 SURFACE QUALITY**

SEM was used to correlate the observed performance results during the PL analysis of Detector 6 and 8. It was shown that Detector 6 produced a brighter intensity than Detector 8. PL intensity is a good indicator of the irregularities in the crystal lattice. A crystal lattice with imperfections in the form of inclusions and defects will lead to trapping of carriers and non-radiative recombination which results in less PL intensity. SEM images of surface shown in Section 5.2.2 confirmed that Detector 8 had a much rougher surface than Detector 6. Detector 8's surface was riddled with small holes.

### **7.4.2 INTERNAL QUALITY**

IR Transmission results showed that the internal structure of Detector 8 was worse than Detector 6 since it had more Te inclusions and a large void. Information from Redlen Technologies showed that Detector 8 was under more strain than Detector 6 (1.8 vs. 1.4, respectively) [19]. A crystal under more strain is more likely to form voids and other irregularities in the crystal lattice. These irregularities have a direct impact on the PL intensity because any voids/defects will act as recombination centers and lead to non-radiative recombination.

## **8 CONCLUSION**

This thesis characterized the optical properties of several CZT semiconductor samples. The samples were from 4% and 10% zinc concentration material and were provided from UVIC Crystal Growth and Redlen Technologies, respectively. The materials were characterized using four different methods which showed supporting results in the experimental data. The findings of the thesis are that 2% Bromine Methanol etch had an improvement on the PL intensity and reduced the XRD line width. This resulted because the polishing and etching smoothed out the surface from defects (XRD improvement) and removed oxidization (PL improvement). In addition, it was confirmed that the performance of Detector 6, compared to Detector 8, was a result of the smoother surface (SEM images) and less irregularities in the crystal lattice (IR

Transmission results). Overall this thesis allowed for an in depth study of the theory of CZT semiconductors and characterization methods. The data obtained can be used to optimize the growing parameters resulting in higher performance CZT crystals in the future.

## 9 REFERENCES

- [1] Redlen Technologies, "PCAMM 2014 Meeting Poster," University of Victoria, 2014.
- [2] H. Chen, S. Awadalla, J. Mackenzie, R. Redden, G. Bindley, A. E. Bolotnikov, G. S. Camarda, G. Carini, R. B. James, "Characterization of Travelling Heater Method (THM) Grown CdZnTe Crystals," *IEEE Transactions on Nuclear Science*, Vol. 54, No. 4, August 2007.
- [3] Ashcroft and Mermin, "Solid State Physics," United States: Cenge Learning, 1976.
- [4] Carleton, "X-Ray Diffraction," [Online serial] 2004, Available: [http://serc.carleton.edu/research\\_education/geochemsheets/BraggsLaw.html](http://serc.carleton.edu/research_education/geochemsheets/BraggsLaw.html)
- [5] G. Sivaranan, "Characterization of cadmium Zinc telluride solar cells," *University of South Florida*, November 12, 2003.
- [6] B. E. A. Saleh and M. C. Teich, "Fundamental of Photonics," United States: Wiley, 2007.
- [7] J. Franc, P. Hlídek, P. Moravec, E. Belas, P. Höschl, L. Turjanska, and R. Varghová, "Determination of energy gap in Cd<sub>1-x</sub>Zn<sub>x</sub>Te (x = 0-0.06)," *Semicond. Sci. Technol.*, vol. 15, no. 6, p. 561, Jun. 2000.
- [8] S. Pereira, M. R. Correia, K. P. O'Donnell, E. Alves, "Interpretation of double x-ray diffraction peaks from InGaN layers," *Applied Physics Letters*, Vol. 79, No. 10, September 2001.
- [9] J. Chu and A. Sher, "Physics and Properties of Narrow Band Semiconductors," New York: Springer, 2008.
- [10] M. Yudong, H. Hui, Q. Juan and C. Hua, "Effects of different surface treatment of CZT sample on the values of DCRC FWHM of X-ray diffraction," *Kunming Institute of Physics*, SPIE Vol. 3553, pp 61-65.
- [11] M. A. Moram and M. E. Vickers, "X-ray diffraction of III-nitrides," *Reports on Progress in Physics*, Vol. 72, pp 40, 2009.
- [12] S. Kochuveedu and D. Kim, "Surface Plasmon Resonance Mediated Photoluminescence Properties of Nanostructured Multicomponent Fluorophore Systems," *Nanoscale*, Vol. 6, pp 4966-4984, 2014.

- [13] MECH 423 Class Notes, *Engineering Ceramics*, Dr. H. King, University of Victoria, Summer 2014.
- [14] Whitman College, “Frank M. Dunnivant Webpage,” [Online Serial], 2015, Available: <http://people.whitman.edu/~dunnivfm/>
- [15] Vahid Brahami. (2015, April 14). *Monochromator Question*. Available e-mail message, University of Victoria.
- [16] MECH 472 Class Notes, *Introduction to Electron Microscopy*, Dr. R. Herring, University of Victoria, Spring 2015.
- [17] Dr. Neil Armour. (2015, April 15). *IR Transmission Theory*. Available e-mail message, University of Victoria.
- [18] Olympus, “Olympus Microscopy,” [Online Serial], 2015, Available: <http://www.olympus-lifescience.com/en/>
- [19] Lindsay Burgess. (2014, December 12). *CZT Alignment*. Available e-mail message, Redlen Technologies.

## 10 APPENDIX A – DCRC MEASUREMENT TECHNIQUE [9]

2.5.1 CHARACTERIZATION OF CRYSTALS 121

The point wise DCRC measurement technique is also used on  $\text{Hg}_{1-x}\text{Cd}_x\text{Te}$  epitaxial films. Figure 2.44 shows such a study on an LPE  $\text{Hg}_{1-x}\text{Cd}_x\text{Te}$  layer grown on a substrate (Zhu 1997). It can be seen from Fig. 2.44 that the rocking curve at the edge of the epitaxial layer is broader than that of the central part. The FWHM values vary in the range of  $\sim 26$ – $47''$ . During the course of LPE growth, the quartz clamp holding the substrate acts as a barrier and results in distortions at the substrate edges. Then different parts of the substrate, such as parts between the center and edges, have different super saturation levels that can affect the quality of the epitaxial layer crystal grown. However, the rocking curves still have a high symmetry and multiple peaks do not emerge, which indicates that this  $\text{Hg}_{1-x}\text{Cd}_x\text{Te}$  film grown by vertical dipping LPE has a uniform structure and good crystal quality.

The FWHM is related to the dislocation revealing etch pit density on the surface of a sample. A FWHM and etch pits density (EPD) study was done for  $\text{Cd}_{0.96}\text{Zn}_{0.04}\text{Te}$  samples, prepared to have different crystal qualities. At least five different zones on each sample were measured and the results averaged to get the data shown in Fig. 2.45. The result shows a strong correlation with EPD's in the range of  $\sim 0.4$ – $4 \times 10^5 \text{ cm}^{-2}$  corresponding to FWHM values of  $\sim 20$ – $60''$ . Thus the dislocation density of CdZnTe can be estimated from a measurement of the FWHM.

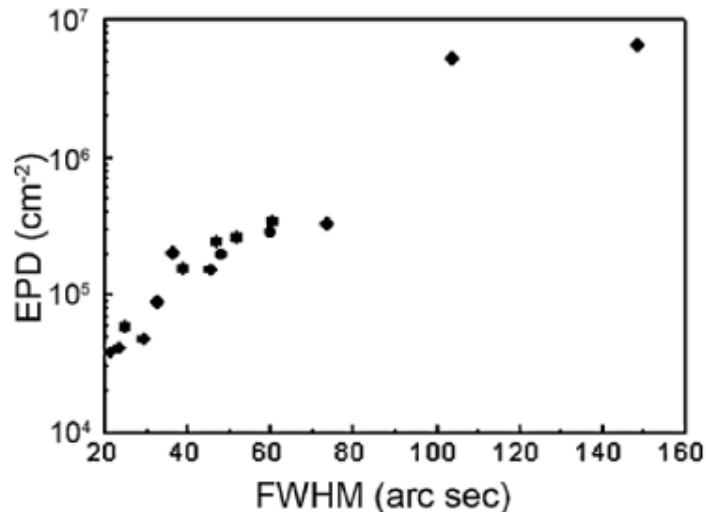


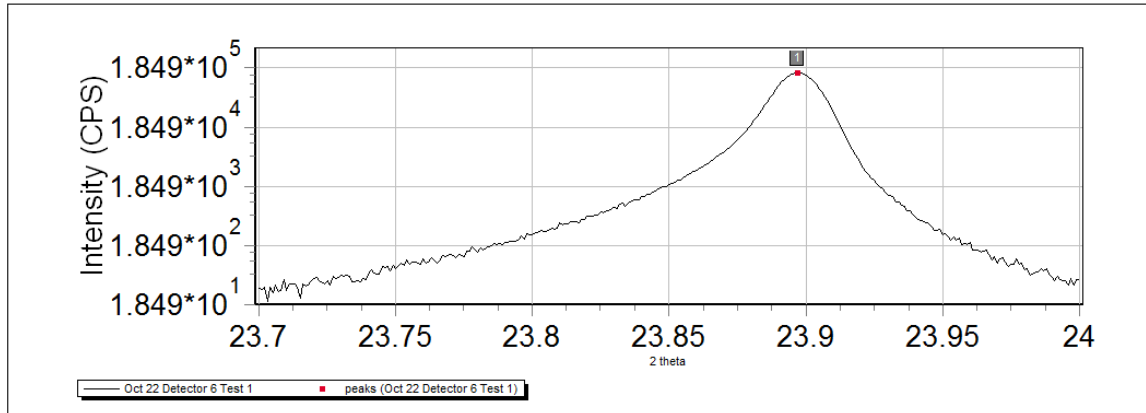
**Fig. 2.45.** FWHM of double-crystals rocking curves for  $\text{Cd}_{0.96}\text{Zn}_{0.04}\text{Te}$  as a function of etch pit density

The dislocation density of a  $\text{Hg}_{1-x}\text{Cd}_x\text{Te}$  epitaxial layer also can be estimated from the FWHM of DCRC experiment. Dislocations in epilayers have several sources:

## 11 APPENDIX B – HRXRD DATA NON ETCHED

### 11.1 DETECTOR 6 NON ETCHED XRD DATA

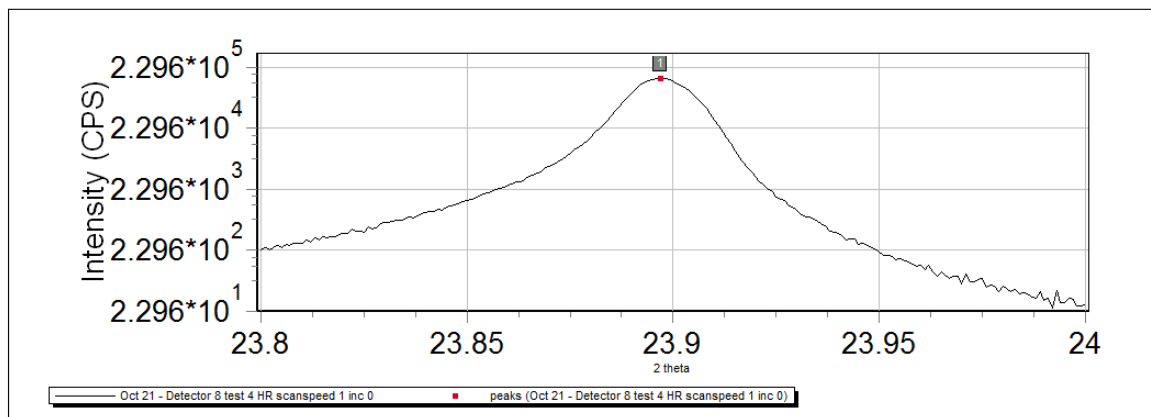
22/10/2014 2:21:20 PM  
 Project:  
 Operator: University of Victoria  
 Sample: r2576  
 Site: Victoria BC, Canada



N	Show	Associate	Label	Layer	Position	Intensity	Mode	FWHM (deg/rlu)	FWHM (sec)	LHM Position	LHM Intensity	RHM Position	RHM Intensity
1	+		1		23.8969	1.516E5	M	0.0172	61.8710	23.8884	75801.8380	23.9056	75801.8380

### 11.2 DETECTOR 8 NON ETCHED XRD DATA

21/10/2014 5:20:19 PM  
 Project:  
 Operator: University of Victoria  
 Sample: r2576  
 Site: Victoria BC, Canada



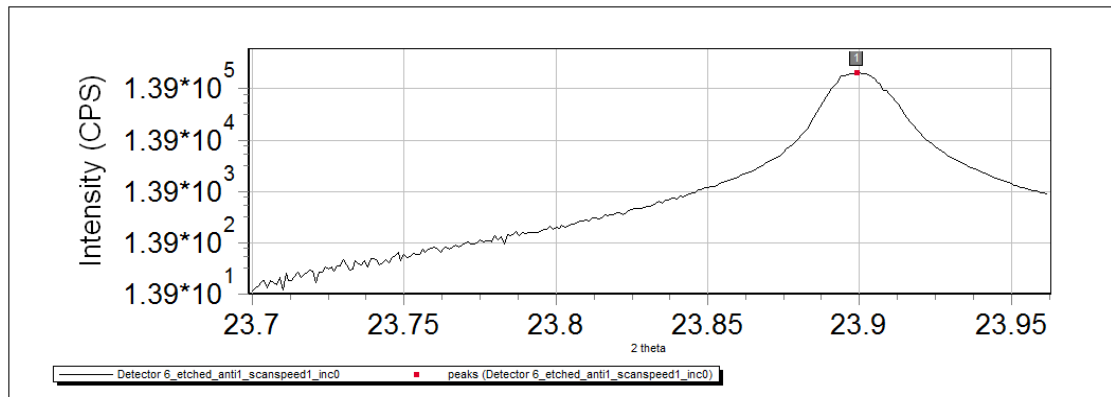
N	Show	Associate	Label	Layer	Position	Intensity	Mode	FWHM (deg/rlu)	FWHM (sec)	LHM Position	LHM Intensity	RHM Position	RHM Intensity
1	+		1		23.8969	1.4894E5	M	0.0166	59.7352	23.8889	74469.2080	23.9055	74469.2080

## 12 APPENDIX C – XRRD DATA ETCHED SAMPLES

### 12.1 DETECTOR 6 ETCHED XRD DATA

19/12/2014 11:36:11 AM

Project:  
Operator: University of Victoria  
Sample:  
Site: Victoria BC, Canada

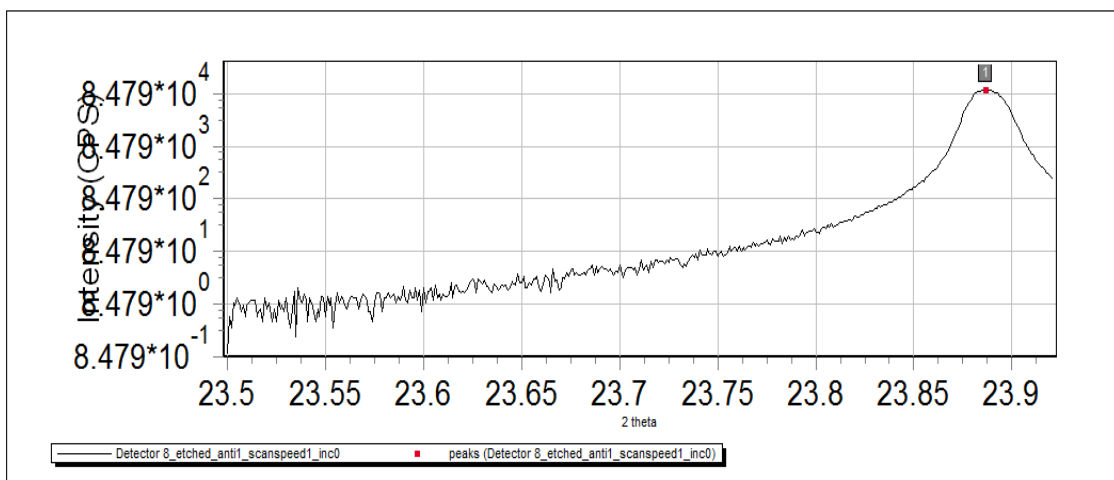


N	Show	Associate	Label	Layer	Position	Intensity	Mode	FWHM (deg/rlu)	FWHM (sec)	LHM Position	LHM Intensity	RHM Position	RHM Intensity
1	+		1		23.893	2.8547E5	M	0.0172	62.0322	23.8909	142735.1800	23.9082	142735.1800

### 12.2 DETECTOR 8 ETCHED XRD DATA

19/12/2014 12:50:03 PM

Project:  
Operator: University of Victoria  
Sample:  
Site: Victoria BC, Canada



N	Show	Associate	Label	Layer	Position	Intensity	Mode	FWHM (deg/rlu)	FWHM (sec)	LHM Position	LHM Intensity	RHM Position	RHM Intensity
1	+		1		23.8869	98341	M	0.0208	74.7962	23.8771	49170.6030	23.8979	49170.6030

### 12.3 SAMPLES 1218-3 ETCHED XRD DATA

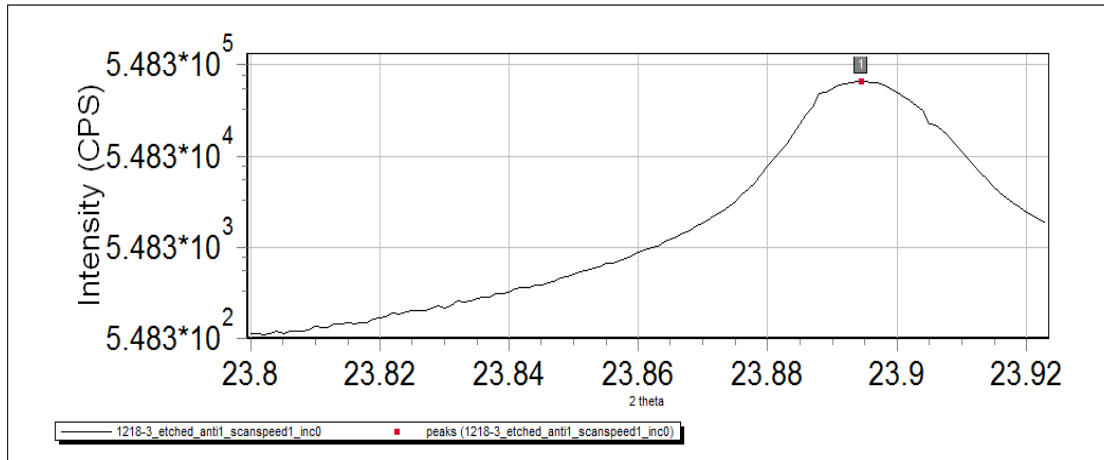
19/12/2014 1:35:20 PM

Project:

Operator: University of Victoria

Sample:

Site: Victoria BC, Canada



N	Show	Associate	Label	Layer	Position	Intensity	Mode	FWHM (deg/rlu)	FWHM (sec)	LHM Position	LHM Intensity	RHM Position	RHM Intensity
1	+		1		23.8945	3.6104E5	M	0.0171	61.4756	23.8864	180517.8900	23.9035	180517.8900

### 12.4 SAMPLE 1527-9 ETCHED XRD DATA

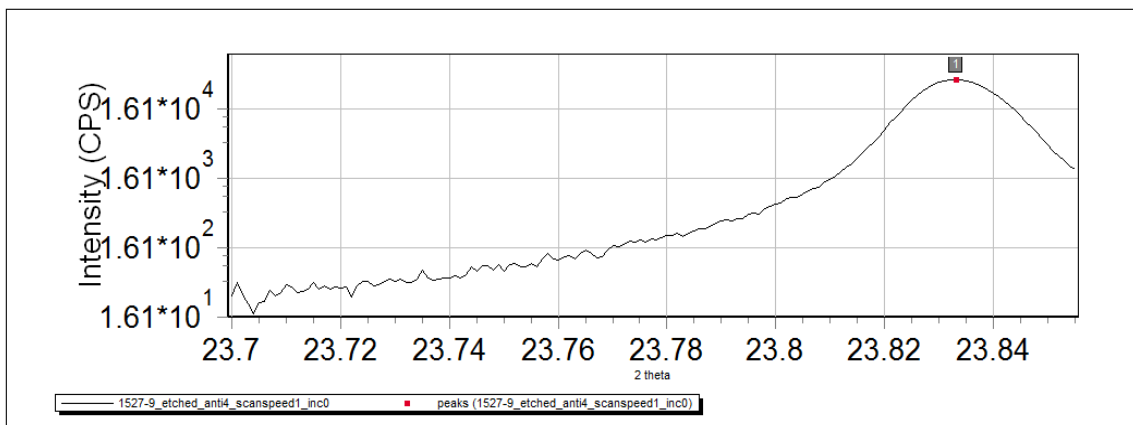
19/12/2014 2:38:55 PM

Project:

Operator: University of Victoria

Sample:

Site: Victoria BC, Canada

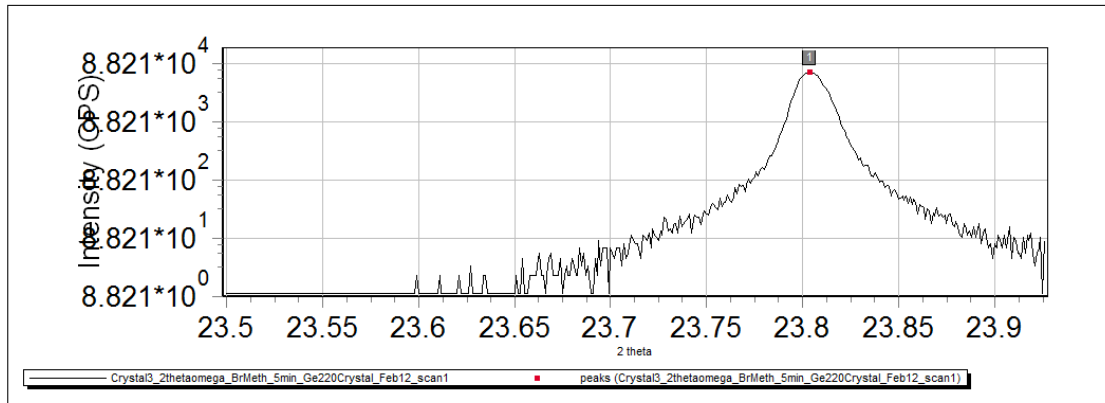


N	Show	Associate	Label	Layer	Position	Intensity	Mode	FWHM (deg/rlu)	FWHM (sec)	LHM Position	LHM Intensity	RHM Position	RHM Intensity
1	+		1		23.8331	42039	M	0.0173	62.1101	23.8248	21019.4390	23.8420	21019.4390

### 13 APPENDIX D – UVIC CRYSTAL GROWTH SAMPLES XRD DATA

#### 13.1 CRYSTAL 3 – 5 MIN 2% BROMINE METHANOL ETCH

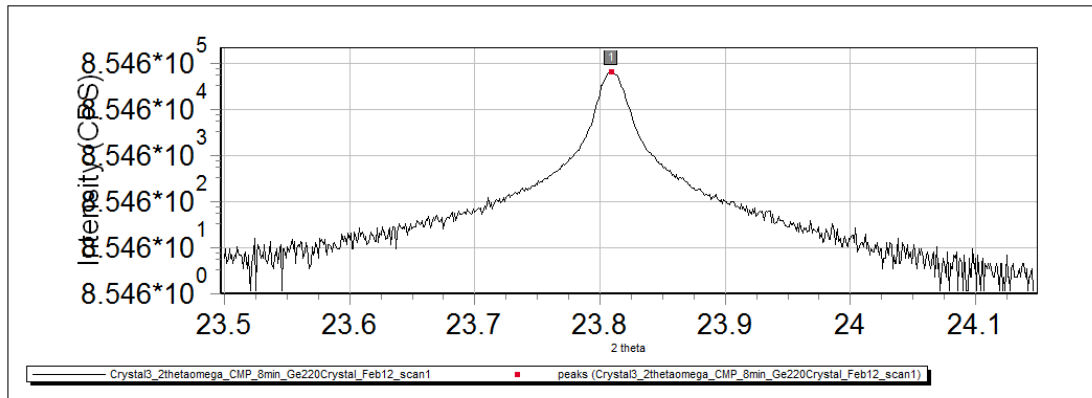
12/02/2015 2:12:01 PM  
 Project:  
 Operator: University of Victoria  
 Sample: r2  
 Site: Victoria BC, Canada



N	Show	Associate	Label	Layer	Position	Intensity	Mode	FWHM (deg/ru)	FWHM (sec)	LHM Position	LHM Intensity	RHM Position	RHM Intensity
1	+		1		23.8038	62220	M	0.0165	59.2732	23.7962	31109.9480	23.8127	31109.9480

#### 13.2 CRYSTAL 3 – 8 MIN 2% BROMINE METHANOL ETCH

12/02/2015 2:11:11 PM  
 Project:  
 Operator: University of Victoria  
 Sample: r2  
 Site: Victoria BC, Canada



N	Show	Associate	Label	Layer	Position	Intensity	Mode	FWHM (deg/ru)	FWHM (sec)	LHM Position	LHM Intensity	RHM Position	RHM Intensity
1	+		1		23.8095	5.6324E5	M	0.0156	56.3399	23.8018	281620.1100	23.8174	281620.1100